



Near-field imaging of optical fibres in the mid-infrared for new Mid-Wave Infrared Fiber Science

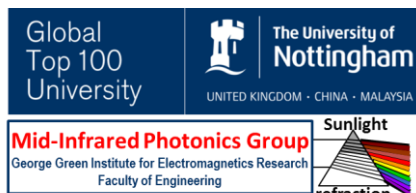
**Angela Seddon
UNIVERSITY OF NOTTINGHAM**

**03/17/2017
Final Report**

DISTRIBUTION A: Distribution approved for public release.

**Air Force Research Laboratory
AF Office Of Scientific Research (AFOSR)/ IOE
Arlington, Virginia 22203
Air Force Materiel Command**

REPORT DOCUMENTATION PAGE				Form Approved OMB No. 0704-0188	
<p>The public reporting burden for this collection of information is estimated to average 1 hour per response, including the time for reviewing instructions, searching existing data sources, gathering and maintaining the data needed, and completing and reviewing the collection of information. Send comments regarding this burden estimate or any other aspect of this collection of information, including suggestions for reducing the burden, to Department of Defense, Executive Services, Directorate (0704-0188). Respondents should be aware that notwithstanding any other provision of law, no person shall be subject to any penalty for failing to comply with a collection of information if it does not display a currently valid OMB control number.</p> <p>PLEASE DO NOT RETURN YOUR FORM TO THE ABOVE ORGANIZATION.</p>					
1. REPORT DATE (DD-MM-YYYY) 17-03-2017		2. REPORT TYPE Final		3. DATES COVERED (From - To) 15 Jul 2014 to 14 Jul 2016	
4. TITLE AND SUBTITLE Near-field imaging of optical fibres in the mid-infrared for new Mid-Wave Infrared Fiber Science				5a. CONTRACT NUMBER	
				5b. GRANT NUMBER FA9550-14-1-0180	
				5c. PROGRAM ELEMENT NUMBER 61102F	
6. AUTHOR(S) Angela Seddon				5d. PROJECT NUMBER	
				5e. TASK NUMBER	
				5f. WORK UNIT NUMBER	
7. PERFORMING ORGANIZATION NAME(S) AND ADDRESS(ES) UNIVERSITY OF NOTTINGHAM UNIVERSITY PARK NOTTINGHAM, NG7 2RD GB				8. PERFORMING ORGANIZATION REPORT NUMBER	
9. SPONSORING/MONITORING AGENCY NAME(S) AND ADDRESS(ES) EOARD Unit 4515 APO AE 09421-4515				10. SPONSOR/MONITOR'S ACRONYM(S) AFRL/AFOSR IOE	
				11. SPONSOR/MONITOR'S REPORT NUMBER(S) AFRL-AFOSR-UK-TR-2017-0017	
12. DISTRIBUTION/AVAILABILITY STATEMENT A DISTRIBUTION UNLIMITED: PB Public Release					
13. SUPPLEMENTARY NOTES					
14. ABSTRACT <p>The funding award was used to purchase a bespoke midinfrared quantum cascade laser (MIR-QCL) for use in far-field and near-field assessment of selenidechalcogenide optical fibers fabricated in-house at the University of Nottingham from glasses melted inhouse. In addition, a cost-effective pixelated pyrometer detector has been bought and commissioned and a far-field optical rig has been constructed and commissioned for use in the near-infrared (NIR) for selenidechalcogenide fiber assessment of numerical aperture. Initial results are reported here together with a full scanning electron microscope imaging and elemental analysis of in-house made selenide-chalcogenide step-index fiber (SIF). However, these initial results reveal a problem in that the NA of the laser source used for far-field must be greater than the NA of the fiber to be tested which can be. Successful near-field NIR assessment is reported here on in-house made selenide-chalcogenide fiber. Future work will hook up the new MIR-QCL with the near- and far-field rigs. The PI also reports novel resonant pumping of rare earth ion doped selenide chalcogenide fiber towards achieving MIR fiber lasing above 4 μm wavelength. We report here on two world records achieved during same time period as the EOARD funding: (i) widest MIR supercontinuum generation in a chalcogenide fiber (published in Nature Photonics 2014) and (ii) lowest optical loss Ge-As-Se chalcogenide fiber, with 80 dB/km minimum loss and MIR transmission through 82 μm of fiber.</p>					
15. SUBJECT TERMS mid-infrared fiber, chalcogenide glasses, MWIR optical fibers, EOARD					
16. SECURITY CLASSIFICATION OF:			17. LIMITATION OF ABSTRACT SAR	18. NUMBER OF PAGES	19a. NAME OF RESPONSIBLE PERSON CUMMINGS, RUSSELL
a. REPORT Unclassified	b. ABSTRACT Unclassified	c. THIS PAGE Unclassified			19b. TELEPHONE NUMBER (Include area code) 011-44-1895-616021



Near-field imaging of optical fibres in the mid-infrared for new Mid-Wave Infrared Fiber Science

FINAL REPORT & COLLATION

14 March 2017

**State-of-the-art,
mid-infrared (3-12 μm wavelength) optical fibers:
optimizing near-field performance, fiber-design and glass-chemistry.**

Professor AB Seddon,

*Mid-Infrared Photonics Group,
George Green Institute for Electromagnetics Research
University of Nottingham, UK.
angela.seddon@nottingham.ac.uk*

CONTENTS	page
Glossary	1
Abstract.	1
1. Technical Proposal- 10 July 2013.	3
2. Two slides provided to EOARD – 2 Feb. 2015.	7
3. Update on Progress provided to EOARD - 18 June 2015.	8
4. Final Report - 14 March 2017.	20

Glossary

CEO	Chief Executive Officer
FTIR	Fourier transform infrared
MIR	mid-infrared
NA	numerical aperture
NIR	near-infrared
OD	outside diameter
QCL	quantum cascade laser
RE	rare earth ion (lanthanide ion)
SIF	step index fiber
SOTS	standard-of-the-shelf
2-D	two-dimensional

Al	aluminum
Ba	barium
Dy ³⁺	dysprosium trivalent cation
F	fluorine, fluoride
La	lanthanum
Na	sodium
Pr ³⁺	praseodymium trivalent cation
SiO ₂	silica
Tb ³⁺	terbium trivalent cation
Zr	zirconium

Abstract

This Report is a collation of the information supplied to EOARD 2014-2017 comprising the original Proposal, intermediate Reports consisting of PowerPoint slides (Feb. 2015) and interim Progress Report (June 2015) and the Final Report. The EOARD funding award (\$50k) was used in its entirety to purchase a bespoke mid-infrared quantum cascade laser (MIR-QCL) for use in far-field and near-field assessment of selenide-chalcogenide optical fibers fabricated in-house at the University of Nottingham from glasses melted in-house. In addition, a cost-effective pixelated pyrometer detector has been bought and commissioned and a far-field optical rig has been constructed and commissioned for use in the near-infrared (NIR) for selenide-chalcogenide fiber assessment of numerical aperture. Initial results are reported here together with a full scanning electron microscope imaging and elemental analysis of in-house made selenide-chalcogenide step-index fiber (SIF). However, these initial results reveal a problem in that the NA of the laser source used for far-field must be greater than the NA of the fiber to be tested which can be > 1 . Successful near-field NIR assessment is reported here on in-house made selenide-chalcogenide fiber. Future work will hook up the new MIR-QCL with the near- and far-field rigs. We also report novel resonant pumping of rare earth ion doped selenide chalcogenide fiber towards achieving MIR fiber lasing above 4 μm wavelength. We report here on two world records achieved during same time period as the EOARD funding: (i) widest MIR supercontinuum generation in a chalcogenide fiber (published in Nature Photonics 2014) and (ii) lowest optical loss Ge-As-Se chalcogenide fiber, with 80 dB/km minimum loss and MIR transmission through 82 m of fiber.

1. Technical Proposal to EOARD, 10 July 2013

1.1. Long-term Aim and Aim of this Proposal

1.2. Relevant Background

1.3. Proposed research tasks and milestones

1.4. Justification of costing

1.5. Suitability of University of Nottingham

References

1.1 Long-term Aim and Aim of this Project

The long-term aim is to create a new paradigm in mid-infrared (MIR) fiberoptic power-output, sensing and imaging. New, MIR fiber-based bright-sources, as well as passive conduit fibers, are key to this aim.

The aim of this Project, is to construct a novel experimental rig for assessing the geometrical arrangement of glass, and MIR modality, of our in-house fabricated MIR fiber, to give us important iterative feedback on MIR fiber design and glass processing.

1.2. Relevant Background

1.2.1 Usefulness of MIR spectral region

There is currently great interest in the MIR spectral region. Soref, a leading contemporary US visionary in photonics and electronics declared in his Jan. 2013 SPIE keynote lecture [1.1]: ‘the mid-infrared is alive!’.

The MIR spectral region is defined as 3-50 μm and covers the important atmospheric windows of 3-5 and 8-12 μm wavelength regions enabling, for example, MIR ship-to-ship free space communications and MIR aircraft free-space counter-measures and collision avoidance. The MIR spectral region also encompasses the molecular fingerprints, that is the characteristic MIR fundamental vibrational absorptions, of numerous gases, liquids and solids as diverse as: combustion gases (giving potential for controlling energy efficiency); ground, water and air pollutants and greenhouse gases (for controlling the environment); pharmaceuticals; toxic agents (for security); soft materials such as plastics and biological tissue (for laser machining and laser surgery and real-time tissue imaging). These matters are discussed further in our papers [1.2, 1.3].

Exploiting the MIR effectively requires the development of a raft of new fiber and waveguide based, narrow and broadband sources, sensors, imaging systems, power delivery and components. An ultimate aim is to achieve analogous flexibility and capability (although not long-haul communications) at the MIR wavelengths as is presently delivered at telecom wavelengths using predominantly silica-glass based fiber [1.2].

For instance to date there are no fiber lasers available for general use beyond 3 μm wavelength.

1.2.2 Suitability and potential of chalcogenide glass fiber-optics for MIR

Chalcogenide glasses provide transparency across the MIR wavelength range and are sufficiently chemically and physically robust materials for development. Chalcogenide glass based optical fibers not only exhibit MIR passive transmission, but also have the potential to be very bright narrow and broadband, MIR fiber-optic sources. The latter would facilitate: free-space communications; new laser machining; new wavelengths for laser medical-surgery; real-time molecular sensing and spectral imaging; MIR coherent imaging and MIR power delivery [2.2]. These are the nuts and bolts of MIR communication systems which could provide real-time molecular information to inform decision-taking in many walks of life and enable greater control to be had in real-time over a diversity of processes.

Achieving MIR fiber lasing is an important step in developing MIR photonics, and this is briefly covered in the following section.

1.2.3 Chalcogenide glass MIR fiber lasers

Commercially available fiber lasers can cover the wavelength range: 400 nm-3 μm . The problems with obtaining longer wavelengths are connected with the host glass material. Lanthanide ions have many photoluminescent transitions in the MIR, but these are quenched by the host material of many currently used fibers [1.3, 1.4]. For example, the most popular material to date for the realization of fiber lasers is silica glass. However, the phonon

energy of silica is 1100 cm^{-1} which is the reason why wavelengths above $2\text{ }\mu\text{m}$ are strongly quenched in this material. In order to construct a MIR fiber laser, a host material with a low phonon energy must be manufactured. A candidate is the chalcogenide glasses, which can have very low phonon energies compared to other glasses used to produce fiber lasers, such as ZBLAN ($\text{ZrF}_4\text{-BaF}_2\text{-LaF}_3\text{-AlF}_3\text{-NaF}$) and silica. We have modelled [1.5] fiber lasers based on Pr^{3+} , Dy^{3+} and Tb^{3+} rare earth ions doped in selenide-chalcogenide glass fibers. Fig. 1, from [1.5], shows the dependence of the output fiber-laser power on the fiber-laser length for selected values of the fiber optical loss. In all cases the doping concentration is 1500 ppmw and the pump power: 5 W. This study shows that significant output power can be achieved even with losses as high as 3 dB/m.

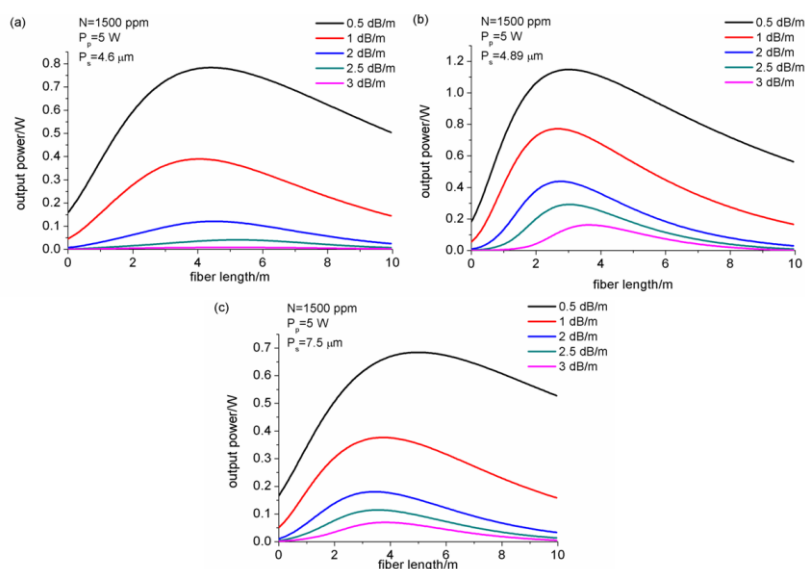


Figure 1.1 Calculated dependence of fiber-laser output power on fiber length for different levels of fiber optical loss for: a) Dy^{3+} ; b) Pr^{3+} and c) Tb^{3+} doped into a selenide-chalcogenide glass fiber [1.5].

1.2.4 Making chalcogenide glass MIR fiber-optics

We make multimode core/clad. passive transmission fiber [1.6] - lowest optical loss $\sim 1\text{ dB m}^{-1}$, cf. the champion optical loss achieved for sulfide-chalcogenide glass optical fibers is 12 dB/km [1.7]. We make fiber monomode in the near-infrared (NIR) (paper (i) in preparation). We have measured MIR photoluminescence in a multimode rare earth ion doped optically-clad fiber (paper (ii) in preparation).

1.2.5 Importance of iterative feedback when making chalcogenide fiber-optics

It is imperative that we have iterative feedback on the MIR fibers we make, in order to optimize our glass processing and fiber-making.

The first step in making chalcogenide optical fiber for MIR active or passive operation is fiber design. Our fiber design capability is based on electromagnetic wave propagation modeling and fiber laser modeling.

To realize the fiber design, the minimum requirements are: (i) low optical loss fiber and (ii) control over the geometry of the finished fiber. For instance, a simple fiber geometry could be a tightly-controlled core-diameter, and core-location, along the fiber length, of a circular core that exhibits guiding in the core.

We measure fiber optical loss in the MIR using the standard cut-back method and FTIR (Fourier transform infrared) spectroscopy which gives us reassuring feedback on our precursor sourcing, glass chemistry, glass processing and fiber fabrication processing routes.

Iterative feedback of the geometrical arrangement and modality of the finished fiber is presently done by imaging fibers in the near-field using SOTS (standard-of-the-shelf) near-infrared (NIR) laser diodes/cameras. This capability is in common with thousands of labs. across the world, for this is the frequency realm of silica glass fiber.

However, SOTS NIR components are not appropriate for fibers destined for MIR use. There are several reasons why not, as follows.

Firstly, chalcogenide glasses exhibit anomalous (steeply changing) refractive index dispersion in the NIR, yet normal refractive index dispersion in the MIR. Secondly, the shorter wavelengths in the NIR that fiber designed and fabricated to be monomode in the MIR ((all other things being equal) would be multimode in the NIR.

In short, the feedback got from measuring NIR near-field fiber propagation and modality is not helpful for successful MIR fiber development and operation. Therefore we wish to measure near-field fiber propagation and modality in the MIR. This is the initial research aim of this Project.

1.3. Proposed research tasks and milestones

To achieve our Project aim of measurement of near-field fiber propagation and modality in the MIR, we shall purchase a suitable MIR laser, detector, and nano-positioner. A focal plane array detector would be ideal but beyond the scope of costing here. Instead we shall buy an entry-level non-monolithic, and as multi-facet as possible, detector and one idea is to develop a 2-D razor-blade-edge technique (to block the light) together with motorized, computerized nano-positioning stage. The stage position will be synchronized with the light detected in order to map the MIR light emitted from a fiber and thereby understand the fiber near-field and fiber geometry. The MIR necessarily means longer wavelengths of operation which means the diffraction limit is larger (unhelpful) but core sizes *etc.* are potentially bigger than for NIR use. Aiming for measurement in the 3-5 μm wavelength region will be helpful because detection is more sensitive there rather than at 5-12 μm .

Task 1 Buying equipment for MIR near-field rig

Source and purchase suitable MIR source(s), detector(s) and nano-positioner(s).

Milestone 1: delivery of source, detector and nano-positioner.

Task 2 Commissioning MIR near-field rig using multimode core/clad. MIR fiber

The source, detector and nano-positioner will be assembled as an optical rig and first tested with a simple multimode core/clad. chalcogenide fiber, whose optical loss spectrum has been measured. The aim is to make good the MIR optical circuit and characterize it for repeatability.

A typical fiber geometry, for a particular fiber draw batch, will be first characterized using analytical scanning electron microscopy (SEM) mapping, as a calibration of the new MIR rig.

We will work out:

- (i) how to raster across the near-field of the exit face of the known multimode fiber;
- (ii) how to capture repeatably, small spatial parts of the exiting light;
- (iii) how to synchronize in time both (i) and (ii), and
- (iv) how to perform this measurement for one fiber reproducibly and so that geometrically it matches what is seen by the SEM mapping calibration. Computer control of the rastering and light acquisition will be carried out using MatLab software.

Milestone 2: repeatable near-field MIR imaging of a multimode core/clad fiber of measured optical-loss and whose geometry has been calibrated by SEM mapping, to $\pm 5 \mu\text{m}$ 2-dimensional (2D) spatial resolution.

Task 3 Pushing equipment to its highest resolution to measure monomode core/clad. fiber and other structured fiber types

Task 3 involves pushing what has been achieved during Task 2 to greater limits of spatial resolution using well characterized monomode core/clad fiber and other structured fibers.

Milestone 3: repeatable near-field MIR imaging of a monomode core/clad fiber whose geometry has been calibrated by SEM mapping, to $\pm 1 \mu\text{m}$ 2D spatial resolution and if possible to 0.5 μm 2D repeatability.

The main aim of this Project will be fundamental scientific results concerning the properties of MIR optical fibers, which we would wish to publish in high impact journals and at conferences. If a successful prototype MIR near-field rig is developed, we would seek to protect the intellectual property associated with a patent.

1.4. Justification of costing

The whole of this budget will be required to purchase the equipment.

1.5. Suitability of University of Nottingham, UK

The University of Nottingham is research-led and ranked as in world's 100 best universities. The University of Nottingham is an elite UK Russell Group university. *updated:* In the last UK Government Research Excellence Framework (REF, December 2014) the University of Nottingham was ranked 8th in the UK. The University of Nottingham is a truly global university with campi in Kuala Lumpur, Malaysia, and Ningbo, China.

The University of Nottingham, UK, is internationally renowned for world-changing, award-winning research and its reputation for excellence attracts distinguished researchers to the staff – many of whom are internationally recognized in their field. The strength of their work lies in their commitment to go beyond traditional boundaries, carrying out research across a vast range of disciplines. Notably, the Nobel Prize was awarded to Sir Peter Mansfield of the University of Nottingham for MRI imaging and medical imaging remains a powerful strand of research at the University.

The MIR Photonics Group lies within the Wolfson Centre for Materials Research with access to a raft of local equipment and broad range of on-campus, state-of-the-art equipment.

1.6. Summary

1.6.1. Background:

Exploiting the MIR demands new MIR fibers and wave-guides for power delivery, narrow and broadband sources, sensors and imaging.

For instance, to date, there are no fiber lasers $\geq 4 \mu\text{m}$ wavelength.

At present, near-field imaging of chalcogenide fiber is in the NIR.

1.6.2. Aim:

Build and commission a novel rig for assessing MIR near-field guiding & modality of passive and active, chalcogenide core/clad. fiber, fabricated at the University of Nottingham, to give iterative feedback on fiber-design, glass-chemistry and glass-processing.

1.6.3. Impact:

Controlling the MIR near-field behaviour is a critical step towards achieving high performance passive and active MIR fibers.


References

- 1.1 Richard Soref, Keynote address: SPIE Photonics West, San Francisco Jan. 2013.
- 1.2 AB Seddon, Int. J. Appl. Glass Sci 2 [3] 177-191 (2011), **Invited Paper**.
- 1.3 AB Seddon, Z Tang, D Furniss, S Sujecki and TM Benson. Optics Express 18 [25] 26704-26719 (2010) **Invited paper**.
- 1.4 L. B. Shaw, B. Cole, P. A. Thielen, J. S. Sanghera, and I. D. Aggrawal, IEEE J. Quantum. Electron. 37 1127 (2001).
- 1.5 L Sójka, Z Tang, H Zhu, E Beres-Pawlik, D Furniss, AB Seddon, TM Benson and S Sujecki, Optical Materials Express 2 [11] 1632-1640 (2012).
- 1.6 SD Savage, CA Miller, D Furniss and AB Seddon, Journal of Non-Crystalline Solids 354 [29] 3418-3427 (2008).
- 1.7 G. E. Snopatin, V. S. Shiryaev, V. G. Plotnichenko, E. M. Dianov, and M. F. Churbanov, Inorg. Mat. 45 [13] 1439–1460 (2009).

2. Two slides provided to EOARD – 2 Feb. 2015


Organization of the layout of these two slides was prescribed by John Gonglewski of EOARD.

2.1: Background, Objective, Impact and Funding.



State-of-the-art, mid-infrared (3-12 μm wavelength) optical fibers: optimizing near-field performance, fiber-design and glass-chemistry.

Professor AB Seddon, Mid-IR Photonics Group, University of Nottingham, UK.

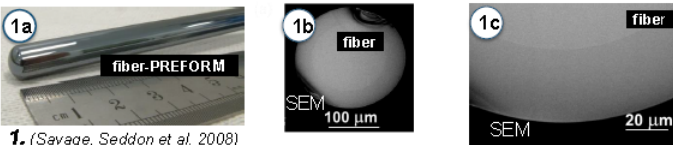


Background:
We are glass chemists & photonics engineers working on new, real-time sensors & imaging to exploit the rich fundamental molecular vibrational absorption across 3-12 μm wavelengths. For this, we fabricate mid-IR fibreoptics. Near-IR near-field imaging (as opposite) is useful.
But no off-the-shelf mid-IR fibre-diagnostics are available.

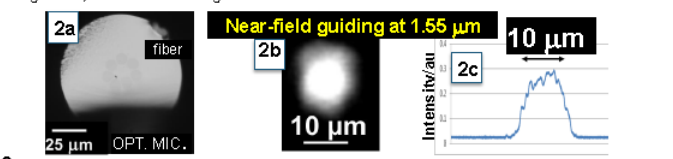
Objective:
Build and commission a novel rig for assessing mid-IR near-field guiding & modality of passive & active, chalcogenide fiber, fabricated primarily at the University of Nottingham, to give iterative feedback on fiber-design & glass-chemistry.

Impact:
Controlling the mid-IR near-field behaviour is a critical step towards achieving high performance passive and active mid-IR fibers for new devices and systems.

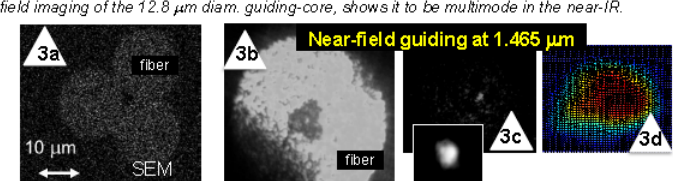
Funding:
24 months (2014-2016)
AFOSR/EOARD \$50k



1. (Savage, Seddon et al. 2008) Large core, core/clad. chalcogenide fiber which is multimode in the near-IR and mid-IR.




2. (Lian, Seddon et al. 2009.) Small-core, microstructured chalcogenide fiber. Near-IR near-field imaging of the 12.8 μm diam. guiding-core, shows it to be multimode in the near-IR.



3. (Li, Seddon et al., paper in preparation. Small-core, micro-structured chalcogenide fiber whose guiding core is 2.2 μm diam..


AFRL 1

2.2 Technical Merits, Relevance, Objectives, Impact (Development Potential), Funding and Key Institution.



State-of-the-art, mid-infrared (3-12 μm wavelength) optical fibers: optimizing near-field performance, fiber-design and glass chemistry.

Professor AB Seddon, Mid-IR Photonics Group, University of Nottingham, UK.



Technical Merits:
New real-time sensors & imaging to exploit the rich, fundamental molecular vibrational absorption across 3-12 μm wavelengths based on mid-IR fibreoptics.
But no off-the-shelf mid-IR fibre-diagnostics are available.

Relevance:
Includes: **security** (detection of: narcotics; explosives; gas, liquid, solid toxic agents); **health in battlefield** (wound healing; bodily "non-well-being" diagnostics) and **new bright sources**: free-space communications & counter-measures.

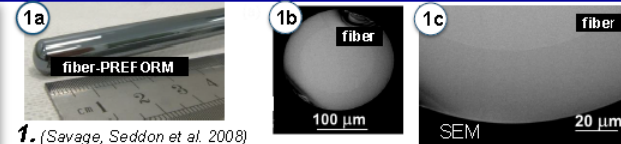
Objective(s):

- Build novel rig to assess fiber mid-IR near-field guiding and modality
- Commission and calibrate rig
- Assess multimode, then monomode, step-index then micro-structured fiber
- Iterate glass chemistry & fibre design


Impact (Development Potential):
Provides understanding of how to translate glass chemistry & fiber design into high performance mid-IR optical systems.

Funding:
24 m (2014-2016) AFOSR/EOARD \$50k

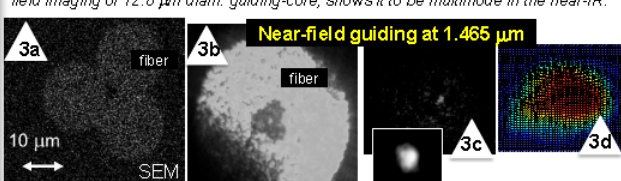
Key Institution:
University of Nottingham, England.



1. (Savage, Seddon et al. 2008) Large core, core/clad. chalcogenide fiber which is multimode in the near-IR and mid-IR.



2. (Lian, Seddon et al. 2009.) Small-core, microstructured mid-IR fiber. Near-IR near-field imaging of 12.8 μm diam. guiding-core, shows it to be multimode in the near-IR.



3. (Li, Seddon et al., paper in preparation. Small-core, micro-structured chalcogenide fiber whose guiding core is 2.2 μm diam..

AFRL 2

3. Update on Progress provided to EOARD - 18 June 2015

3.1 Aim and objectives

3.2 Progress on grant objectives to 18 June 2015

3.3 Recent publications and citations

References

Appendix I	Design and Build of optical rig.
Appendix II	Theory of light guiding in fiber and numerical aperture.
Appendix III	AB Seddon publication list: 2014 -2015.

3.1 Aim and objectives

The overall aim of this research is to build and commission a novel, mid-infrared (MIR) optical rig for the characterization of mid-infrared (MIR) optical fibers.

The objectives are:

- (i) build optical rig;
- (ii) calibrate then test optical rig in near-infrared (NIR), in particular NIR numerical aperture (NA);
- (iii) source and buy MIR quantum cascade laser (QCL)
- (iv) source and buy inexpensive MIR arrayed detector;
- (v) test optical rig in MIR; measure MIR NA of fiber; capture MIR near-field images of fiber and MIR modality; test out effectiveness of mode-stripping solutions.

3.2 Progress on grant objectives to 18 June 2015

Objective (i): Build optical rig (for characterization of MIR optical fiber)

Appendix I contains more details about building the optical rig built in-house. Figs. 3.1 to 3.3 illustrate the rig comprises:

- a rotating stage supporting the detector and
- an optical fiber holder supported on an adjustable platform which is held on a breadboard and solid stage.

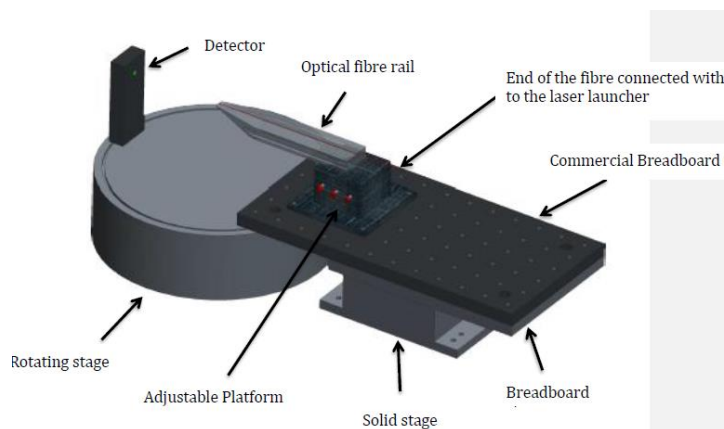


Figure 3.1 Optical rig designed and built in-house for measuring MIR fiber NA.

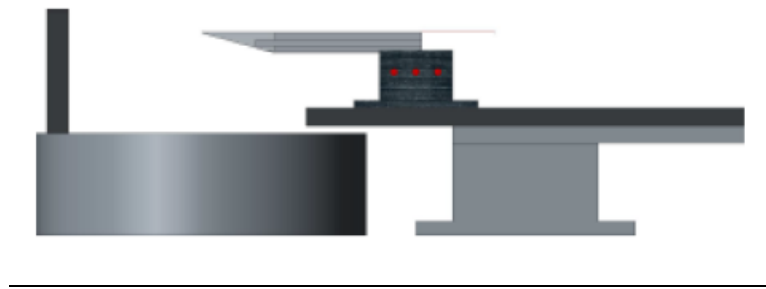


Figure 3.2 Side elevation of the apparatus shown in Fig. 1 for measuring MIR fiber NA.

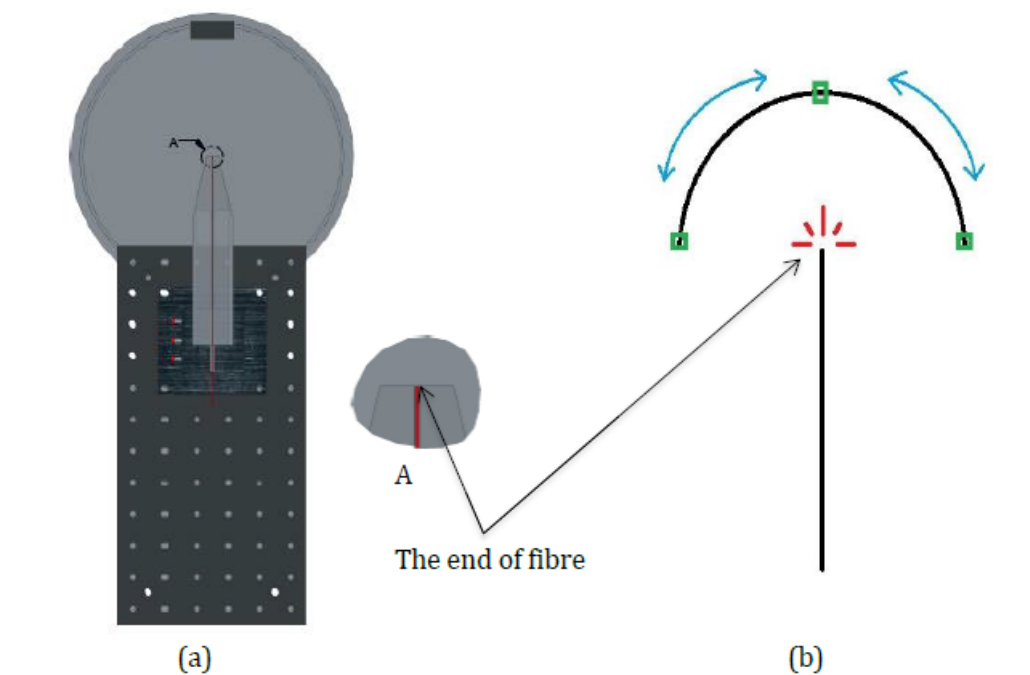


Figure 3.3 (a) Demonstration of how fiber set up and (b) how detector moves.

Objective (ii): Calibrate then test MIR fiber optical rig in near-infrared (NIR) in particular NIR numerical aperture (NA)

The built optical rig was calibrated using a 980 nm laser diode source (Covega, now supplied by Thorlabs) and two types of silica-glass optical fibers:

- British Telecom Standard silica-glass optical fiber and
- multimode silica-glass optical fiber.

Figs. 3.4 and 3.5 show plots of the intensity of exit light *versus* angle of detector, with respect to the fiber axis, for the BT Standard and multimode fiber, respectively.

Fig. 3.4 shows a smooth response for the BT Standard fiber. Fig. 3.5 shows a less smooth response for the multimode fiber. As no modal stripping was done in the experiment, it is likely that the extra intensity at larger angle, manifesting as waviness of the intensity response of the plot in Fig. 3.5, was due to higher order modes leaving the cladding glass.

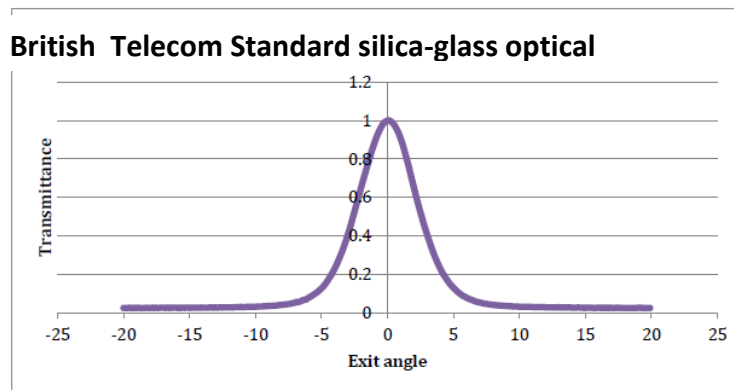


Figure 3.4 Intensity of exit light from BT Standard fiber at different detector capture angles.

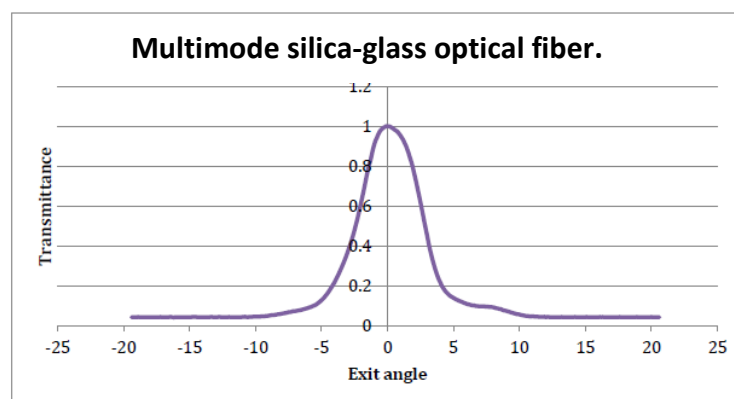


Figure 3.5 Intensity of exit light multimode silica fiber at different detector capture angles.

Using the numerical approach shown in Appendix II, both fibers were calculated to have NA= 0.09. This indicates that the core and cladding glasses of the two fiber types were apparently similar. The British Telecom Standard optical fiber comprised a pure silica glass cladding and germania-doped core.

Objective (iii) source and buy MIR quantum cascade laser (QCL) and inexpensive MIR arrayed detector

We are still examining QCL options to purchase. Our drivers are:

- Output power
- Wavelength

Output power

We wish to purchase a high power QCL for greater versatility of use.

Daylight Solutions, USA, (Laser 2000 is UK agent) have informed us that Export Licence requirements preclude them delivering ≥ 1 W QCLs to UK. Pranalytica, USA, (ELUXI Ltd. is UK agent) anticipate no such problem and cite their recent deliveries inside Europe.

Wavelength

- Near-field imaging MIR fibers: of interest is 3-12 μm wavelength range.
- Biological wavelengths are of interest to us and are at ~ 3 μm wavelength and $>\sim 6$ μm wavelength.
- Other aspects also are driving our wavelength choice.

This has delayed the purchase, as we have debated on the best way forward to achieve greatest versatility of the purchased QCL. We met with Prof Kumar (CEO of Pranalytica, USA) on his visit to the UK Tuesday 16 June 2015 to have more discussion and have requested two new quotes.

Objective (v) source and buy inexpensive MIR arrayed detector

Received MIR arrayed bolometer but not yet commissioned.

3.3 Recent publications and citations

The highlight of our recent work has been to achieve a world record in wideband MIR supercontinuum light from a specially designed MIR optical fiber made at the University of Nottingham, UK.

This work has now been published in Nature Photonics November 2015 (*Mid-infrared supercontinuum covering the 1.4–13.3 μm molecular fingerprint region using ultra-high NA chalcogenide step-index fiber*, CR Petersen, U Møller, I Kubat, B Zhou, S Dupont, J Ramsay, T Benson, S Sujecki, N Abdel-Moneim, Z Tang, D Furniss, A Seddon and O Bang, NATURE PHOTONICS, 8 (2014) 830–834, doi:10.1038/nphoton.2014.213)

This paper **was selected for Nature Photonics New&Views 8 (2014) (NATURE PHOTONICS | VOL 8 | NOV. 2014 | 814-815) where Gr Steinmeyer and Julia S. Skibina wrote: “The demonstration of chalcogenide fiber-based supercontinuum sources that reach beyond a wavelength of ten micrometres is set to have a major impact on spectroscopy and molecular sensing.”**

Other publications include optimizing small-core optical fibers for best MIR photoluminescence published in Optics Express and world record lowest loss for a chalcogenide fiber GeAsSe in Optics Materials Express, as follows:

1) (H Sakr, D Furniss, Z Tang, L Sojka, NA Moneim, E Barney, S Sujecki, TM Benson and AB Seddon. Superior photoluminescence (PL) of Pr^{3+} -In, compared to Pr^{3+} -Ga, selenide-chalcogenide bulk glasses and PL of optically-clad fiber, Optics Express, Vol. 22, Issue 18, pp. 21236-21252 (2014)).

2) (Z Tang, D Furniss, M Fay, H Sakr, Lucasz Sojka, N Neate, N Weston, S Sujecki, TM Benson and AB Seddon, Mid-infrared photoluminescence in small-core fiber of praseodymium-ion doped selenide-based chalcogenide glass, Optical Materials Express 5 (4) 870-886 (2015)).

3) Z Tang, VS Shiryayev, D Furniss, L Sojka, S Sujecki, TM Benson, A B Seddon and Mikhail F. Churbanov, Low loss Ge-As-Se chalcogenide glass fiber, fabricated using extruded preform, for mid-infrared photonics, accepted for publication, 17 June 2015, Optical Materials Express.

Section 3. APPENDIX I

Design and Build of optical rig

i Design description

To measure the dependence of the light intensity on exit angle from a MIR optical fiber, it is necessary to design and make several parts. Here, two components were fabricated inhouse *viz.*: a solid stage and an optical fiber rail. A breadboard stage and breadboard platform were sourced commercially. Figs. i to iv show how the basic components fit together.

ii Components

1. Solid stage
2. Breadboard stage (commercial)
3. Optical fiber rail
4. Breadboard platform (commercial)

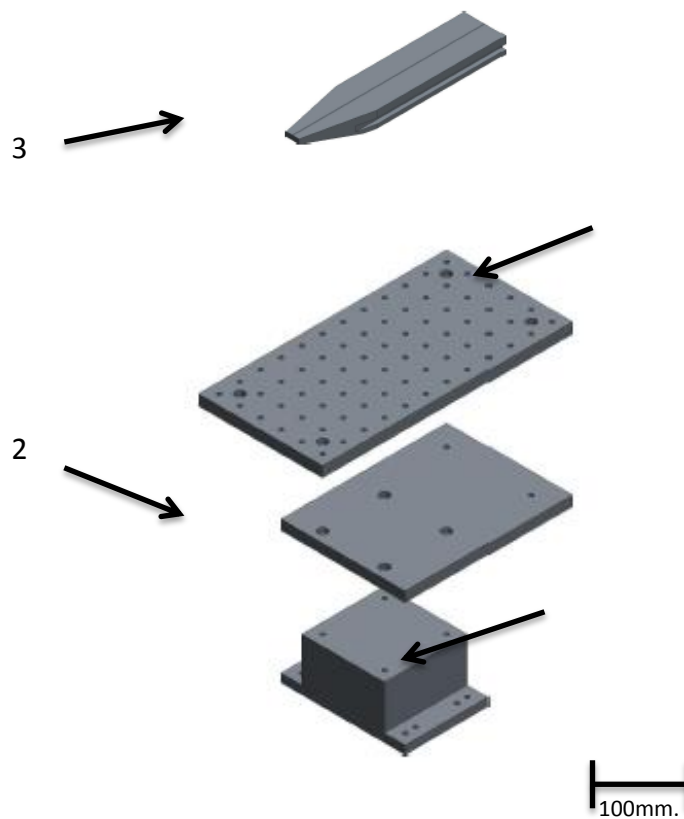


Figure i. Components for the optical rig.

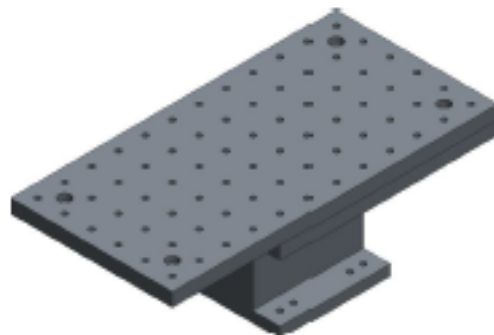


Figure ii. General assembly of solid stage and commercial breadboard stage and breadboard platform for the optical rig.

iii Solid stage.

The purpose of the solid stage was for supporting the breadboard stage. Aluminum was chosen to make the solid stage, being sufficiently stiff, exhibiting high fracture stress and ease of machining. The solid stage was designed to be rigid and adjustable in increments. For the top surface, all holes were “M6 x 1 tapped for 20 mm depth”, while the holes at the bottom surface were “6 mm. diameter through holes”. The critical point was that the table in the laboratory had “25 mm” hole-to-hole and the 3-axis stage that was to be used to hold optical fiber on the breadboard could be adjusted only ± 12.5 mm. Therefore, the holes at the bottom surface had to be “12.5 mm” different from the nearby hole to allow the optical fiber be moved of total “25 mm”. Also, the end of the stage was made into a flat shape, so it could be positioned at any increment by using clamps in case of any special circumstances.

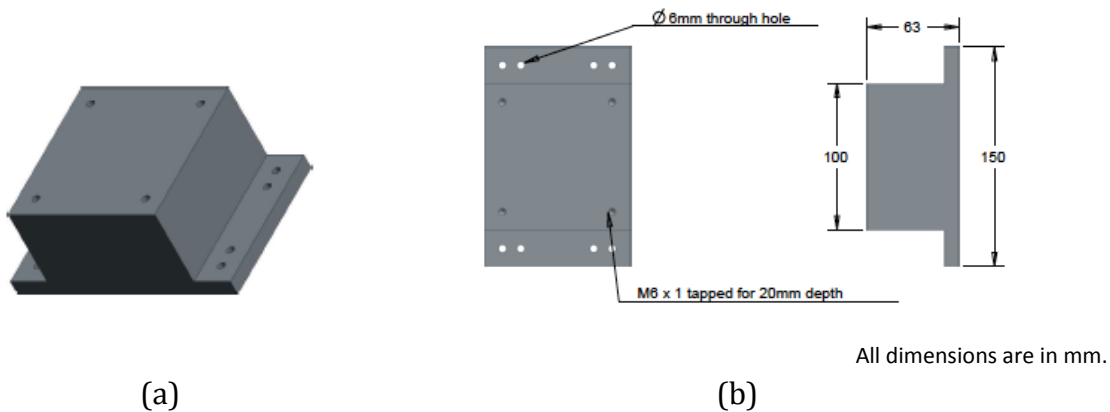


Figure. iii (a) 3D model of the solid aluminum stage and (b) the basic dimensions of the solid aluminum stage.

iv Breadboard stage

The purpose of the breadboard stage was to be able to mount this onto the solid stage. The critical point was to make sure that the height of the breadboard stage combined with the height of the solid stage would exceed the height of the pancake, cantilevered stage. This allowed the end of optical fiber, which was on a breadboard, to be placed above the middle of the pancake, cantilevered stage.



Figure iv. Plan view of the difference in height of the pancake cantilevered stage compared to that of the breadboard stage combined with the solid stage.

The breadboard stage was made from aluminum in order to be light and robust. The breadboard contained two “M6 x 1 tapped through holes” and four counter bolts for “M6 x 1”.

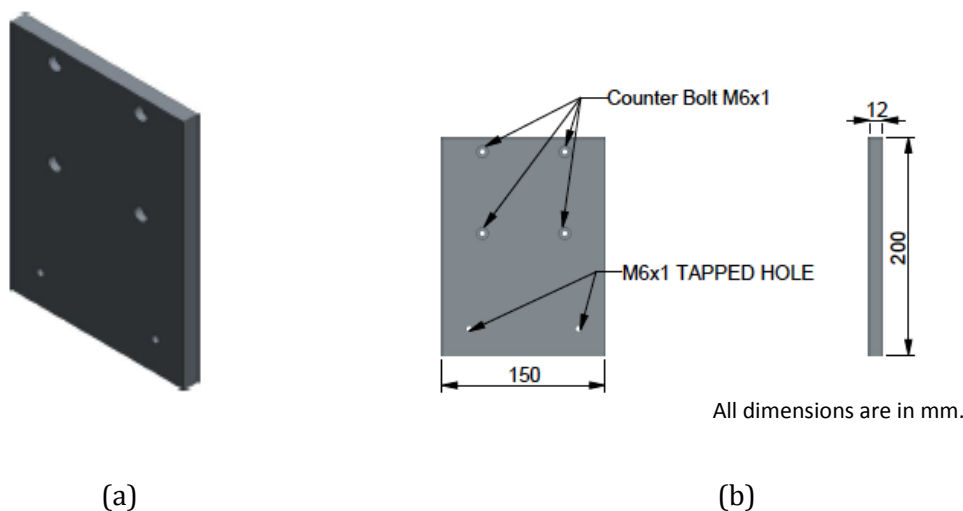


Figure v. (a) 3D model of the breadboard stage and (b) basic dimensions of the breadboard stage.

v Optical fiber rail

An optical fiber rail was used to locate the optical fiber in the position where the detector could measure the intensity with respect to the exit angle from an optical fiber. The groove on top of the rail allowed the optical fiber to lie horizontally and straight axially. The base of the optical fiber rail was designed to be compatible and functional with an ordinary 3-axis stage. Magnets were used to hold the optical fiber in the groove. Therefore, the optical fiber rail had to be made of steel, a magnetic material.

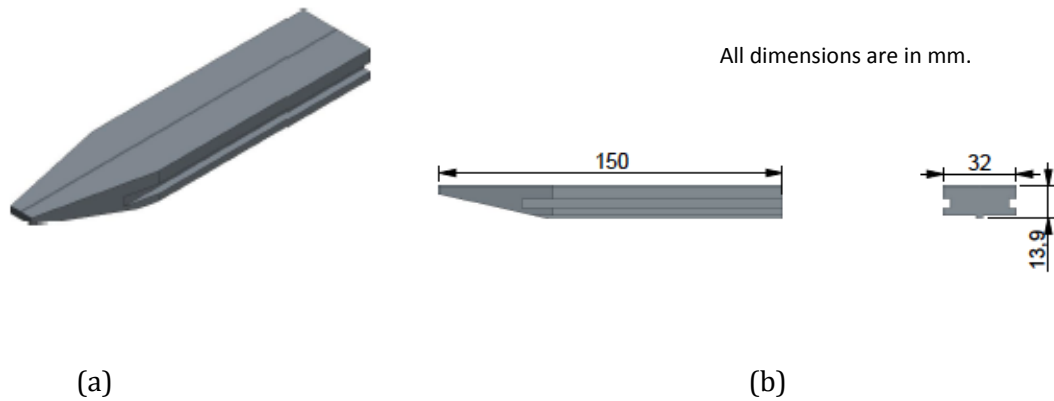


Figure vi. (a) 3D model of the optical fiber rail and (b) basic dimensions of the optical fiber rail.

Section 3. APPENDIX II

1. The basic theory of light guiding

The basic theory to explain how light, which is a form of electromagnetic wave, propagates within the optical fiber is as follows. Normally, intensity and phase of electromagnetic waves have to be investigated by applying Maxwell's equations [I]. Light has a very short wavelength, about 10^{-6} m. For the sake of simplicity here, Maxwell's equations are neglected and a basic concept of light rays are used to describe how light can be guided in the optical fiber [I]. This theory consists of simple physics' concepts and mathematical equations.

1.1 Refraction and reflection inside the optical fiber¹.

Consider the refraction and reflection of light at the boundary of two different refractive index materials. By abruptly changing the refractive index at a boundary, the theory can be described by Snell's law and total internal reflection. Consider the two following cases. First, refractive index n_1 is less than refractive index n_2 ($n_1 < n_2$). When an incident ray is projected into the boundary between two different refractive index media, the incident ray is transmitted into the second medium and also changes its direction. The refraction angle can be represented in Snell's law (equation i and see Fig. i for definition of angles).

Snell's Law:
$$\frac{\sin \theta_1}{\sin \theta_2} = \frac{n_2}{n_1} \quad (i)$$

For the second case, where $n_1 > n_2$, as θ_2 increases, θ_1 will be increased and until θ_2 becomes 0° at a certain angle of θ_1 . At this point, there will be no incident ray transmitted into the second material and all the energy will also be reflected at the boundary. This angle is called the critical angle or the total-reflection complementary angle, θ_c . When the incident ray angle exceeds the critical angle, no ray is transmitted into second medium

For the complementary angle θ_1 and θ_2 :

$$\frac{\cos \theta_1}{\cos \theta_2} = \frac{n_2}{n_1} \quad (ii)$$

where $\theta_2 = 0$ and $\theta_1 = \theta_c$.

$$\frac{\cos \theta_c}{\cos 0} = \frac{n_2}{n_1} \quad (\text{iii})$$

where, $\cos 0 = 1$

$$\theta_c = \cos^{-1} \frac{n_2}{n_1} \quad (\text{iv})$$

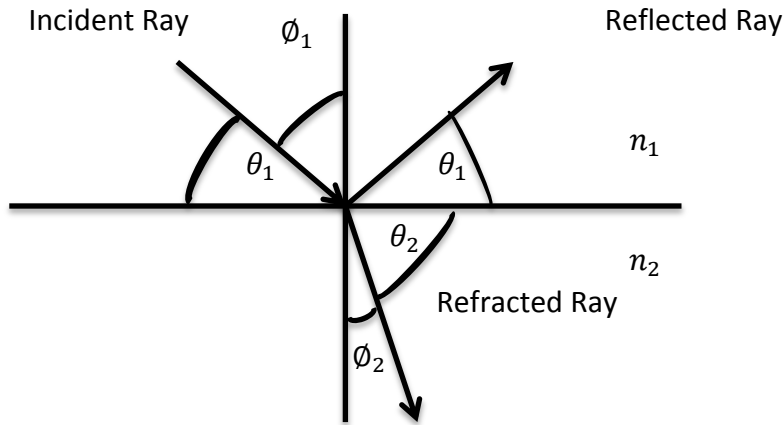


Figure i. Geometric optical light rays at a boundary. Here ϕ_1 and ϕ_2 are the angles made by incident ray and refracted ray respectively with the normal to the interface.

1.2 Numerical aperture (NA)

The electromagnetic wave, or light, will be transmitted along an optical fiber when it enters the optical fiber within the acceptance angle. Numerical aperture (NA) is a dimensionless number used to describe the maximum angle that the electromagnetic wave or light can be transmitted into optical fiber so that total internal reflection occurs inside the fiber. NA can be defined as

$$NA = n_0 \sin \theta_{max} \quad (\text{v})$$

where θ_{max} is the maximum angle that light can be transmitted into optical fiber and contributes to the total internal reflection; n_0 is the refractive index of the medium outside the optical fiber.

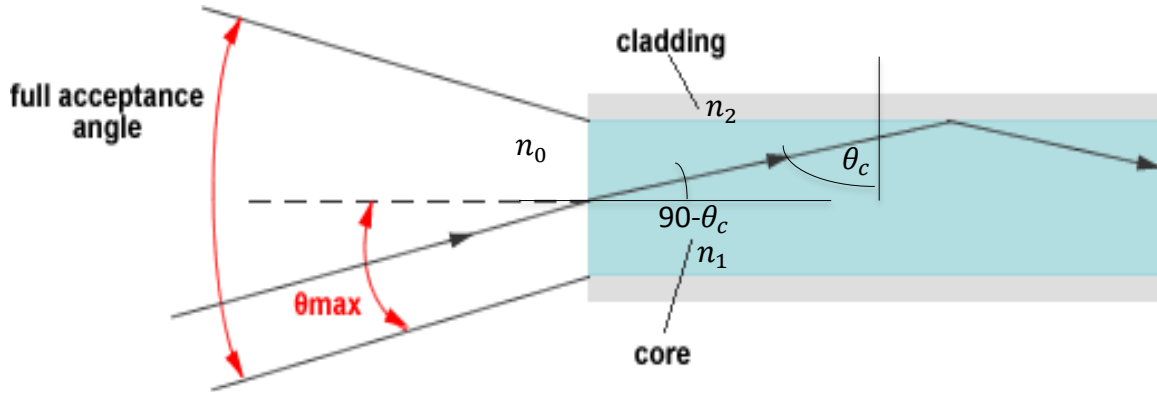


Figure ii. The light enters optical fiber within θ_{max} and the critical angle θ_c .

Due to the reflection between the boundary of outside air and the core of optical fiber, the light ray changes its angle as it enters the core. From Eq. (I and v):

$$NA = n_0 \sin \theta_{max} = n_1 \sin \theta \quad (vi)$$

where θ is the angle of ray inside optical fiber with the normal to the interface between the outside and the core of optical fiber, and n_1 represents refractive index of the core.

$$NA = n_1 \sin \theta \quad (vii)$$

$$NA = n_1 \sin(90 - \theta_c) \quad (viii)$$

$$NA = n_1 \cos \theta_c \quad (ix)$$

Note that: $\cos^2 \theta = 1 - \sin^2 \theta$

$$NA = n_1 \sqrt{1 - \sin^2 \theta} \quad (x)$$

The critical angle can be calculated from Snell's law when θ_2 is 90° and $\theta_1 = \theta_c$. From Eq. (i) and n_2 represents as refractive index of the cladding.

$$\frac{\sin \theta_c}{\sin 90} = \frac{n_2}{n_1} \quad (xi)$$

From Eq. (x) and Eq. (xi):

$$NA = n_1 \sqrt{1 - \left(\frac{n_2}{n_1}\right)^2} \quad (xii)$$

$$NA = \sqrt{n_1^2 - n_2^2} \quad (xiii)$$

n_1 and n_2 are the refractive index of the core and the cladding respectively.

1.3. How can light be transmitted along optical fiber? ¹

Consider when θ_{max} is small and subsequently the angle θ becomes smaller than the angle of $90 - \theta_c$ (where θ_c is the critical angle). Then total internal reflection occurs inside the optical fiber and the ray continues to transmit along the core. Since all the subsequent reflections happen at the same angle, so there is no loss of energy.

On the other hand, when θ_{max} is greater and subsequently θ becomes bigger than the angle of $90 - \theta_{critical}$, then the energy that is transmitted as rays is deteriorated by refraction into the cladding. After numbers of successive refraction, the energy of light becomes smaller and finally being absorbed by cladding

References

I. W. A. Gambling, *Introduction To Optical Fiber Communications*, John Wiley & Sons, Inc., Canada, 1982.

Section 3. APPENDIX III

AB Seddon publication list: 2014, 2015.

- 3.1 I Kubat, C Rosenberg Petersen, U Møller, **AB Seddon**, TM Benson, L Brilland, D M'echin, PM Moselund and O Bang, Thulium pumped mid-infrared 0.9-9 μ m supercontinuum generation in concatenated fluoride and chalcogenide glass fibers, | Vol. 22, No. 4 | **Optics Express** 2 (4) 3959-3967 (2014).
- 3.2 E. A. Romanova, Y. S. Kuzutkina, A. I. Konyukhov, N. Abdel-Moneim, **A. B. Seddon**, T. M. Benson, S. Guizrd and A Mouskeftaras, Nonlinear optical response and heating of chalcogenide glasses upon irradiation by ultrashortlaser pulses, **Optical Engineering** 53 (7) 071812 July 2014 (available on-line Feb 2014).
- 3.3 L Sojka, Z Tang, D Furniss, H Sakr, A Oladeji, E Beres-Pawlik, H Dantanarayana, E Faber, **AB Seddon**, TM Benson and S Sujecki, Broadband, mid-infrared emission from Pr³⁺ doped GeAsGaSe chalcogenide fiber, optically clad, **Optical Materials Express** 36 1076-1082 (2014).
- 3.4 I Kubat, C Rosenberg Petersen, U Møller, **AB Seddon**, TM Benson, L Brilland, D M'echin, PM Moselund and O Bang, Thulium pumped mid-infrared 0.9-9 μ m supercontinuum generation in concatenated fluoride and chalcogenide glass fibers, **Optics Express** 22 (4) 3959-3967 (2014).
- 3.5 A Oladeji, L Sojka, Z Tang, D Furniss A Phillips, **AB Seddon**, TM Benson and S Sujecki, Numerical investigation of mid-infrared emission from Pr³⁺ doped GeAsGaSe fiber, **Opt. Quant. Electron.** 46 (4) 593-602 (2014).
- 3.6 E A Romanova, YS Kuzutkina, AI Konyukhov, N Abdel-Moneim, **AB Seddon**, TM Benson, S. Guizrd and A Mouskeftaras, Nonlinear optical response and heating of chalcogenide glasses upon irradiation by ultrashortlaser pulses, **Optical Engineering** 53 (7) 071812 (2014).
- 3.7 H Sakr, Z Tang, D Furniss, L Sojka, NA Moneim, E Barney, S Sujecki, TM Benson and **AB Seddon**, Towards mid-infrared fiber-lasers: rare earth ion doped, indium-containing, selenide bulk glasses and fiber. **Proc. SPIE** 8938 Optical Fibers and Sensors for Medical Diagnostics and Treatment Applications XIV 89380V (February 20, 2014); doi:10.1117/12.2039405.
- 3.8 JH Butterworth, D Jayasuriya, QQ Li, D Furniss, NA Moneim, E Barney, S Sujecki, TM Benson, JS Sanghera and **AB Seddon**, Towards mid-infrared supercontinuum generation: Ge-Sb-Se mid-infrared step-index small-core optical fiber. **Proc. SPIE** 8938 Optical Fibers and Sensors for Medical Diagnostics and Treatment Applications XIV Feb 2014.
- 3.9 S Sujecki, A Oladeji, L Sojka, A Phillips, **AB Seddon**, TM Benson, H Sakr, Z Tang, D Furniss, K Scholle, S Lamrini and P Furberg. Modelling and design of MIR chalcogenide glass fiber lasers. **Proc. NUSOD** 2014, 14th International Conference on Numerical Simulation and Design of MIR chalcogenide devices, 1-4 September 2014.
- 3.10 Z Tang, D Furniss, M Fay, N Neate, Y Cheng, E Barney, L Sojka, S Slawomir, T Benson and **AB Seddon**, First identification of rare earth oxide nucleation in chalcogenide glasses and implications for fabrication of mid-infrared active fibers. **J. Am. Ceram. Soc.** 97 (2) 432-441 (2014). Article first published online: 12 DEC 2013, DOI: 10.1111/jace.12732.
- 3.11 **AB Seddon**, NS Abdel-Moneim, ZG Lian, WJ Pan, D Furniss, CJ Mellor, T Kohoutek, J Orava, T Wagner and TM Benson. Mid-infrared integrated optics: versatile hot embossing of mid-infrared glasses for on-chip planar waveguides for molecular sensing. **Optical Engineering** (SPIE pub). 53 (7) 071824 2014 doi: 10.1117/1.OE.53.7.07 1824.
- 3.12 HG Dantanarayana, N Abdel-Moneim, Z Tang, L Sojka, S Sujecki, D Furniss, **AB Seddon**, I Kubat, O Bang, and TM Benson, Refractive index dispersion of chalcogenide glasses for ultra-high numerical-aperture fiber for mid-infrared supercontinuum generation. **Optical Materials Express** 4(7) 1444-1455 (2014). DOI:10.1364/OME.4.001444.
- 3.13 Irnis Kubat, Christian S. Agger, Uffe Møller, **Angela B. Seddon**, Zhuoqi Tang, Slawomir Sujecki, Trevor M. Benson, David Furniss, Samir Lamrini, Karsten Scholle, Peter Fuhrberg, Bruce Napier, Mark Farries, Jon Ward, Peter M. Moselund, and Ole Bang, Mid-infrared supercontinuum generation to 12.5 μ m in large NA chalcogenide step-index fibers pumped at 4.5 mm, **Optics Express** 22(16) 19169-

- 19182 (2014). DOI:10.1364/OE.22.01914119169. **This paper was selected for NATURE PHOTONICS Highlights: Maria Maragkou 'Reaching the Mid-infrared light' NATURE PHOTONICS 8, 746 (2014) doi:10.1038/nphoton.2014.231, Published online 01 October 2014**
- 3.14 H Sakr, D Furniss, Z Tang, L Sojka, NA Moneim, E Barney, S Sujecki, TM Benson and **AB Seddon**. Superior photoluminescence (PL) of Pr^{3+} -In, compared to Pr^{3+} -Ga, selenide-chalcogenide bulk glasses and PL of optically-clad fiber. **Optics Express**, 22 (18) 21236-21252 (2014).
- 3.15 CR Petersen, U Møller, I Kubat, B Zhou, S Dupont, J Ramsay, T Benson, S Sujecki, N Abdel-Moneim, Z Tang, D Furniss, **A Seddon** and O Bang, Mid-infrared supercontinuum covering the 1.4–13.3 μm molecular fingerprint region using ultra-high NA chalcogenide step-index fiber, **NATURE PHOTONICS**, 8 (2014) 830–834, doi:10.1038/nphoton.2014.213. **This paper was selected for Nature Photonics New&Views (NATURE PHOTONICS | VOL 8 | NOV. 2014 | 814-815) Gr Steinmeyer and Julia S. Skibina "The demonstration of chalcogenide fiber-based supercontinuum sources that reach beyond a wavelength of ten micrometres is set to have a major impact on spectroscopy and molecular sensing."**
- 3.19 Z Tang, D Furniss, M Fay, H Sakr, Lucasz Sojka, N Neate, N Weston, S Sujecki, TM Benson and **AB Seddon**, Mid-infrared photoluminescence in small-core fiber of praseodymium-ion doped selenide-based chalcogenide glass **Optical Materials Express** 5 (4) 870-886 (2015).

4. Final Report – 14 March 2017

4.1 Aim

4.2 Progress in brief

4.3 Purchase and commissioning of mid-infrared quantum cascade laser (MIR-QCL) source and pixelated pyrometer detector

4.3.1 MIR-QCL

4.3.2 Pixelated pyrometer detector

4.4 Far-field analysis and scanning electron microscopy of mid-infrared transmitting selenide-chalcogenide fiber

4.4.1 Introduction

4.4.2 Methodology

4.4.3 Results and Discussion

4.5 Near field analysis of mid-infrared transmitting selenide-chalcogenide fiber

4.6 Novel resonant pumping of rare earth ion doped selenide-chalcogenide fiber

4.1. Aim

An original aim of this research was to commission a novel, mid-infrared (MIR) optical rig for assessing passive and active, MIR fiber, fabricated at the University of Nottingham, UK, to give iterative feedback on our fiber-design and glass-chemistry.

4.2 Progress in brief

A new optical rig for far-field optical fiber analysis was built and commissioned in the near-infrared (NIR) on commercially-sourced silica-glass optical fibers as described in **Section 3** of this Report.

Following this, the far-field rig has been used to characterize the numerical aperture (NA) of mid-infrared-transmitting selenide-chalcogenide glass fibers which were fabricated in-house (**see section 4.4**). This has been combined with scanning electron microscope analysis of these fibers. The fibers were mainly composed of core and cladding glasses arranged as step-index fibers (SIF) and the refractive index dispersion of these fibers has been checked using outsourced MIR ellipsometry.

The EOARD grant funding was used to purchase a MIR quantum cascade laser (QCL) source and pixelated MIR pyrometer detector; these have been commissioned (**see section 4.3**).

The MIR-QCL source and pixelated MIR pyrometer detector are to be used both in the newly constructed far-field rig (**see Section 3** above of this Report and **section 4.4** below) and our existing near-field rig for fiber analysis (**section 4.5**).

The MIR-QCL source has been used for resonant pumping of our active rare earth ion doped selenide-chalcogenide fibers in research (see **section 4.6**, **Section 4 Appendix I** and **reference [4.1]**) aimed at achieving MIR fiber lasing at $\geq 4 \mu\text{m}$ wavelength. This work was published in January 2017 [4.1].

4.3 Purchase and commissioning of mid-infrared quantum cascade laser (MIR-QCL) source and pixelated pyrometer detector

4.3.1 MIR-QCL

We considered sourcing the mid-infrared quantum cascade laser (MIR-QCL) source from Pranalytica or Daylight Solutions; both companies are headquartered in the USA.

We selected Pranalytica as the Supplier of the MIR-QCL for the following reasons:

- (i) the cost was considerably lower than the quote from Daylight solutions for (nominally) the same kit;
- (ii) Pranalytica guaranteed the wavelength output range ($4.15 \pm 0.05 \mu\text{m}$) and output power of 1 Watt that we required, and
- (iii) Professor Kumar (Chief Executive Officer of Pranalytica) visited us at the University of Nottingham, UK, to discuss our requirements.

Pranalytica delivered the MIR-QCL equipment about 8 months after the order was placed by us. The MIR-QCL source was delivered to the University of Nottingham, UK, from Pranalytica in early 2016. The MIR-QCL source from Pranalytica was commissioned and the output was as specified.

However, after a few weeks the equipment failed due to failure of the integral cooling unit. We were in direct contact with Prof. Kumar, CEO Pranalytica, and instructed to package the equipment and courier it back to Pranalytica for fixing. The MIR-QCL was eventually returned within 2 months to the University of Nottingham, UK, in full working order from Pranalytica.

Thus at the time of writing this Report we have had the MIR-QCL in-house for < 12 months.

4.3.2 Pixelated pyrometer detector

The pixelated pyrometer detector has a wavelength detector range of $\sim 2 - 8 \mu\text{m}$ with lessening detectivity reaching \sim zero at $10 \mu\text{m}$ wavelength. It is a 63×62 array of pixels and is having to be slightly reconfigured for our use. In particular, each pixel must be programmed to have the same threshold detection.

4.4 Far-field analysis and scanning electron microscopy of mid-infrared transmitting selenide-chalcogenide fiber

4.4.1 Introduction:

Building and commission of the far-field rig was described in Section 3 of this Report ('Update to EOARD: 18 June 2015') but **was inaccurately referred to there as a 'near-field' rig rather than the correct 'far-field'.**

Commissioning of the far-field rig, at that time, was carried out in the near-infrared (980 nm source) with silica-glass standard telecommunications, monomode-fiber and silica-glass multimode fiber. Fiber numerical aperture (NA) was determined at 980 nm. In brief, light from a laser-diode source was launched into the cleaved input-face of the optical fiber under-test whilst keeping the cleaved exit-face of the optical fiber static and then moving the power detector in an arc around the exit-face in order to measure the light intensity emitted from the fiber output face at different angles. The measured exit-half-angle was $\pm 5^\circ$ for both fibers and hence the apparent NA of each of both fibers was calculated to be 0.09.

The method was next used to analyze selenide-chalcogenide optical fiber made in-house at the University of Nottingham, UK, and dependence of light-intensity on exit angle was determined at $1.54 \mu\text{m}$ wavelength.

4.4.2 Methodology

The experimental set-up for finding the dependence of light-intensity on exit angle from the selenide-chalcogenide fiber was as follows, in order to calculate the fiber numerical aperture (NA).

There were seven important features in order to set-up the experiment and measure the results (see Fig. 4.1):

- 1 Signal Generator
- 2 Laser Controller
- 3 Laser Launcher
- 4 Chalcogenide Fiber
- 5 Detector
- 6 Amplifier
- 7 Lock-in Amplifier

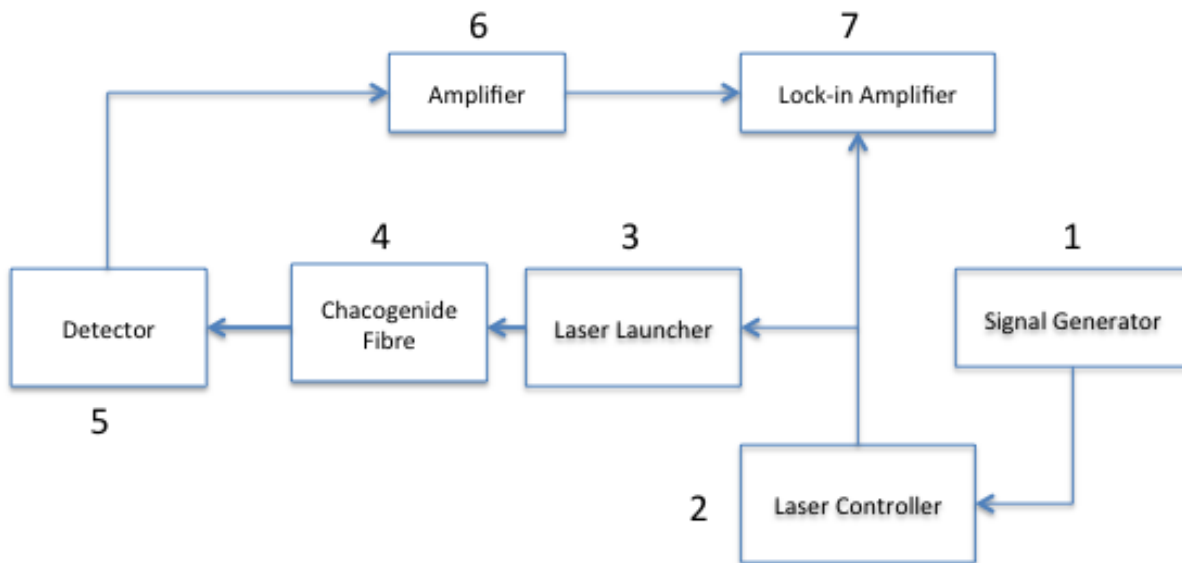


Figure 4.1 Optical circuit for launching and detecting the NIR signal for far-field assessment of fiber.

Firstly, the signal generator was used to create a plus signal, then the signal was transmitted to the laser controller for generating power to drive the laser. After that, the signal was sent to the laser launcher and the lock-in amplifier. The laser launching optics created the laser light and transmitted it to the fiber. The detector was rotated around the end of the fiber to collect the laser intensity at the end of the fiber over the different exit angles. The minimum angle increment used was 0.1° . The intensity of the laser was detected at the detector and transferred to the amplifier. The amplifier amplified the signal from the detector and transmitted the signal to the lock-in amplifier. The lock-in amplifier only collected signals from the detector that had the same frequency as the signal being sent from the signal generator to eliminate any disturbance or any other signals possibly coming from the environment (*sic. – as in stated in Final Year Project Report of undergraduate Vipant Chayavichitsilp, Faculty of Engineering, University of Nottingham, UK*).

Measuring NA and intensity of the light coming out of the fiber, the signal generator was set as the following:

- Using pulse signal (On and Off)
- Frequency = 107 Hz
- Time constant = 1 second
- Sensitivity = $10 \text{ mV} \times 50$

The light source was a tunable laser: $1.465 - 1.575 \mu\text{m}$ (Agilent; 8164B). $1.54 \mu\text{m}$ light was launched using a tapered silica-fiber, mounted on a XYZ translation stage, with focused spot size $2.5 \mu\text{m}$ at the selenide-chalcogenide fiber launch-end. Each selenide chalcogenide fiber was $\sim 1 \text{ m}$ long and the other end of the fiber was placed in the optical fiber rail (see figs. 4.2 and 4.3). As the near-infrared beam was traveling along the fiber and exiting the end of the fiber, the detector was rotated around the end of the fiber to measure the intensity at different exit angles of the fiber.

Far-field analysis of silica glass optical fiber and mid-infrared transmitting selenide-chalcogenide fiber was carried out, that is the dependence of light-intensity on exit-angle of was measured. Previously (see Section 3) the commercially sourced silica-glass based optical fibers: British Telecom standard fiber and the multimode telecom. fiber, were measured across their output intensity within the angle from -10° to $+10^\circ$ with increment 0.1° .

The selenide-chalcogenide fibers to be analyzed had been fabricated in-house and were coded: F007MINSCGNM and F008MINSCGNM, which were each step-index fibers (SIF) of core/cladding glasses = As-Se / Ge-As-Se; also P020 (As-Se) fiber and F018 (Ge-Sb-Se) fiber were analyzed.

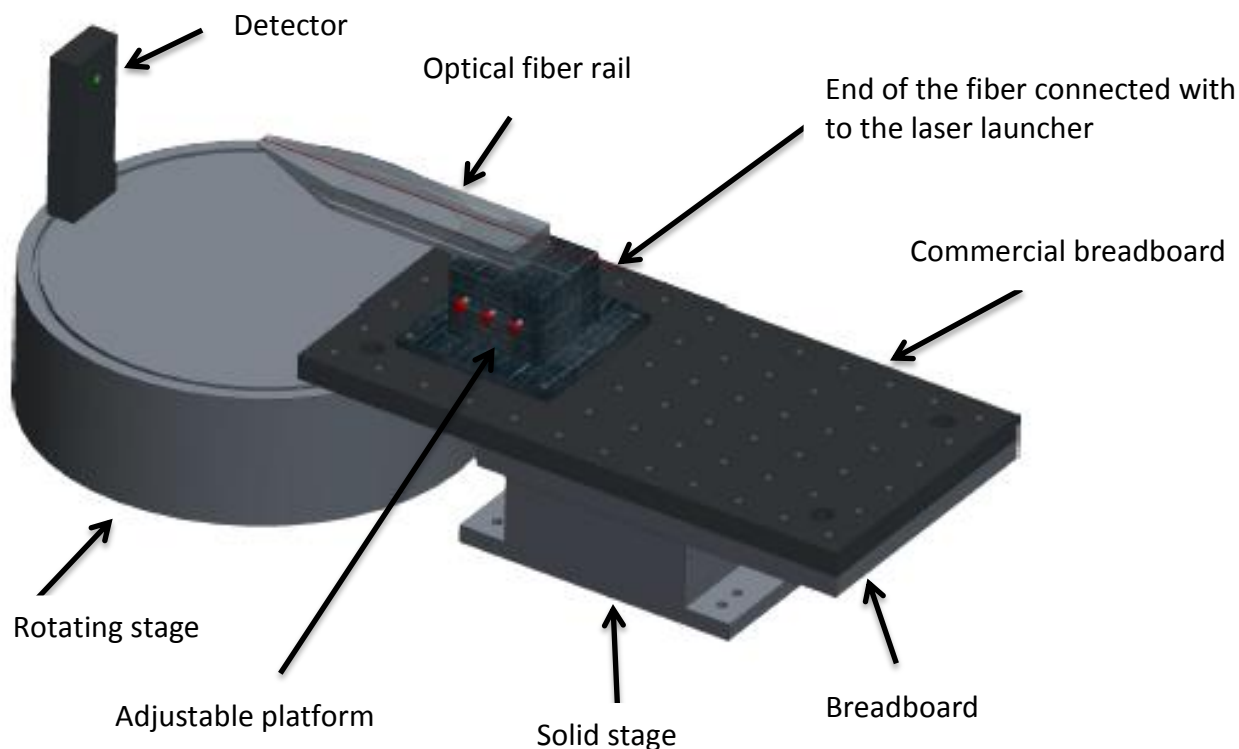


Figure 4.2 Basic components that were used in measuring NIR light intensity exiting at the end of the chalcogenide glass fiber (see Fig. 4.3).

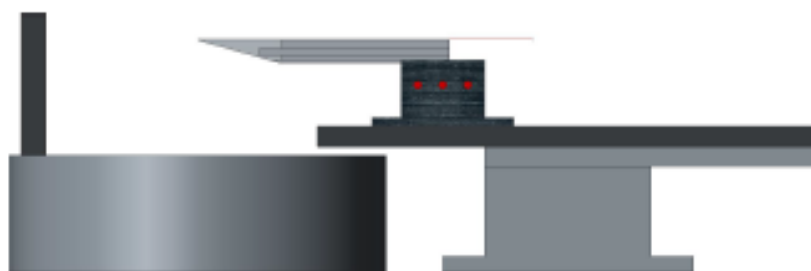


Figure 4.3 Side elevation of the apparatus in Figure 4.2.

F007MINSCGNM and F008MINSCGNM were measured with an increment of 0.1° angle. For F007MINSCGNM, the exiting light intensity was measured from -40° to $+40^\circ$; the intensity at 800 different angles was investigated. Similarly, for F008MINSCGNM, the exiting light intensity was measured from -60° to $+60^\circ$ so the intensity at 1200 different angles was measured. The intensity of the exit light was measured from -40° to $+40^\circ$ for the P020 and -50° to $+50^\circ$ for the F018 SIF. Therefore, the intensity from 800 different points were collected for the P020 $\text{As}_{40}\text{Se}_{60}$ and 1000 points for the F018 SIF.

For each fiber type, the intensity of light emission across the field of view was measured several times to check for reproducibility. Thus, the measurement was repeated four times for the P020 and three times for each of F018, F007MINSCGNM and F008MINSCGNM.

Scanning electron microscopy (SEM) imaging was used to measure the outer and core diameters of each F007MINSCGNM and F008MINSCGNM fiber sample of the selenide-chalcogenide mid-infrared-transmitting

fibers. SEM energy dispersive X-ray spectroscopy (EDS) was applied to each fiber type in order to measure the actual glass composition of the core and cladding glass of each fiber.

4.4.3 Results and Discussion

Firstly the SEM imaging and analysis are presented for the two selenide-chalcogenide fibers: F007MINSCGNM and F007MINSCGNM and then the far-field imaging results are presented for these two fibers, and also for P020 and F018 selenide-chalcogenide fibers.

4.4.3.1. Results of SEM imaging and analysis of F007MINSCGNM

The F007MINSCGNM core/cladding = As-Se/Ge-As-Se large-core step-index fiber was cleaved and six sample cross-sections were investigated using SEM imaging and analysis. Only one sample is shown in each case as an example.

SEM images of F007MINSCGNM core/cladding = As-Se/Ge-As-Se large-core step-index fiber are shown in Figs. 4.3 and 4.4.

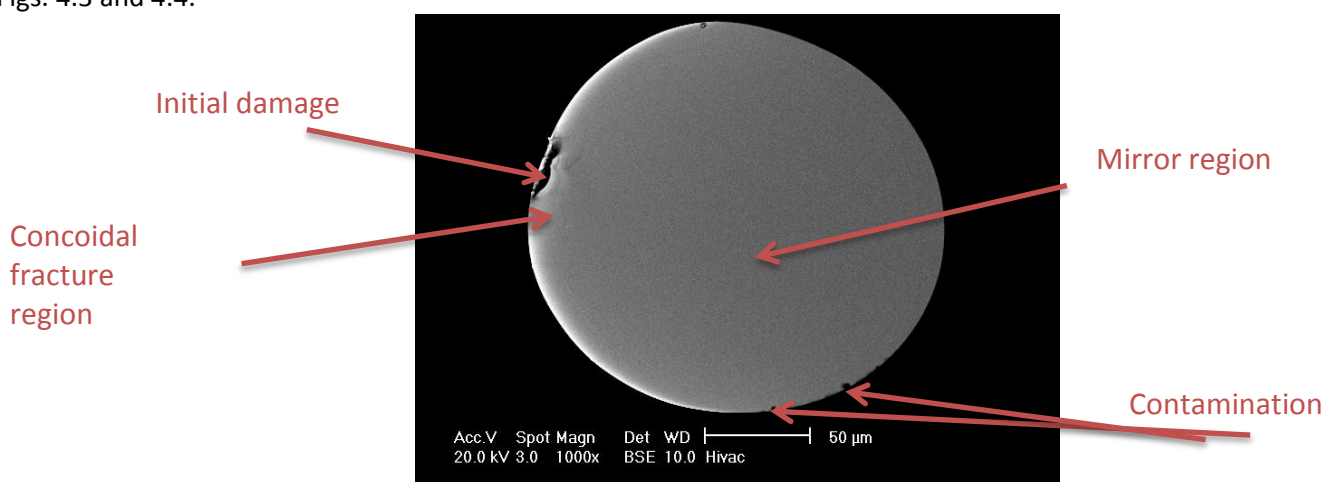
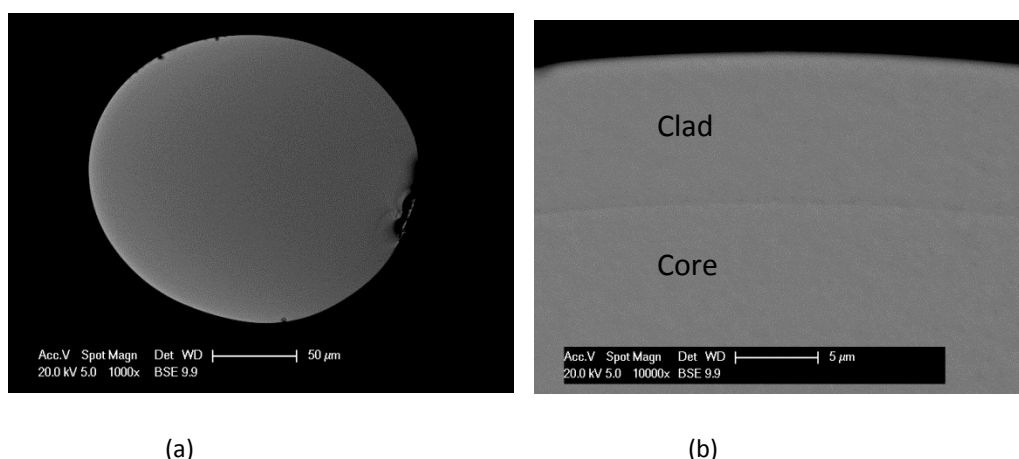


Figure 4.3 SEM imaging of F007MINSCGNM large-core step-index fiber.



(a)

(b)

Figure 4.4. F007MINSCGNM large-core step-index fiber: (a) boundary between the core/cladding. and (b) at higher magnification.

The core diameter and outside diameter (OD) of the F007MINSCGNM large-core step-index fiber have been measuring using SEM. Each diameter was measured two times in a different orientation (see Fig. 4.5) and the average values were calculated (Table 4.1).

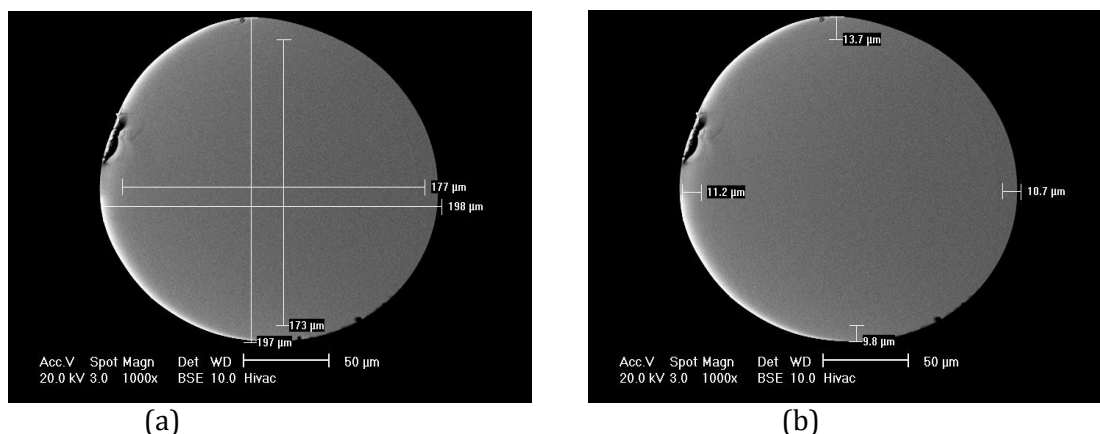


Figure 4.5 F007MINSCGNM large-core/clad fiber: (a) lines for measuring the mean core diameter and (b) lines for measuring average OD.

Table 4.1 Average and standard deviation dimensions of six fiber samples of F007MINSCGNM large-core step-index fiber.

Fiber sample	Average OD / μm	Average core diameter / μm	Average cladding thickness / μm
1	196.5 ± 1.5	175.0 ± 3	10.9 ± 0.9
2	197.5 ± 0.5	175.0 ± 2	11.4 ± 1.2
3	203.5 ± 2.5	177.0 ± 0	12.3 ± 1.3
4	202.5 ± 1.5	179.0 ± 2	11.9 ± 0.8
5	198.0 ± 0	173.5 ± 0.5	11.7 ± 0.7
6	196.0 ± 2	173.0 ± 2	11.2 ± 0.9

In the SEM imaging, it was difficult to see the core/cladding boundary interface of the F007MINSCGNM large-core step-index fiber. There was some adventitious surface contamination on the F007MINSCGNM fiber and some mechanical damage at the fiber outer surface leading to errors in calculating percent asymmetry, which was not attempted.

SEM-EDS elemental mapping of the F007MINSCGNM fiber large-core step-index fiber showed three elements were present: As, Ge and Se. As and Se were depleted in the cladding and Ge was only present in the cladding, as expected (see Fig. 4.6). The elemental composition of both the core and cladding compositions in the F007MINSCGNM fiber were within 1.18 atomic % absolute of the nominal as-batched glass compositions (see Figs. 4.7 and 4.8 and Tables 4.2 and 4.3).

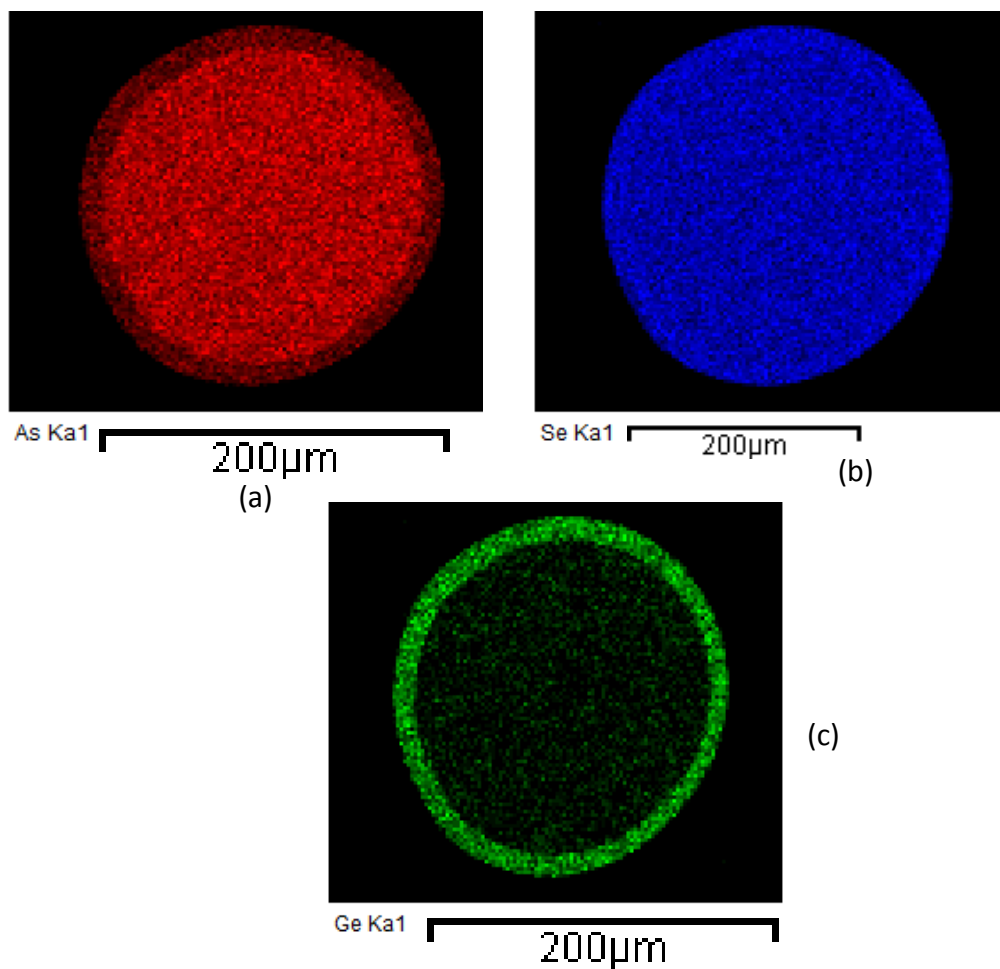


Figure 4.6. F007MINSCGNM fiber large-core step-index fiber: elemental mapping of: (a) As; (b) Se and (c) Ge.

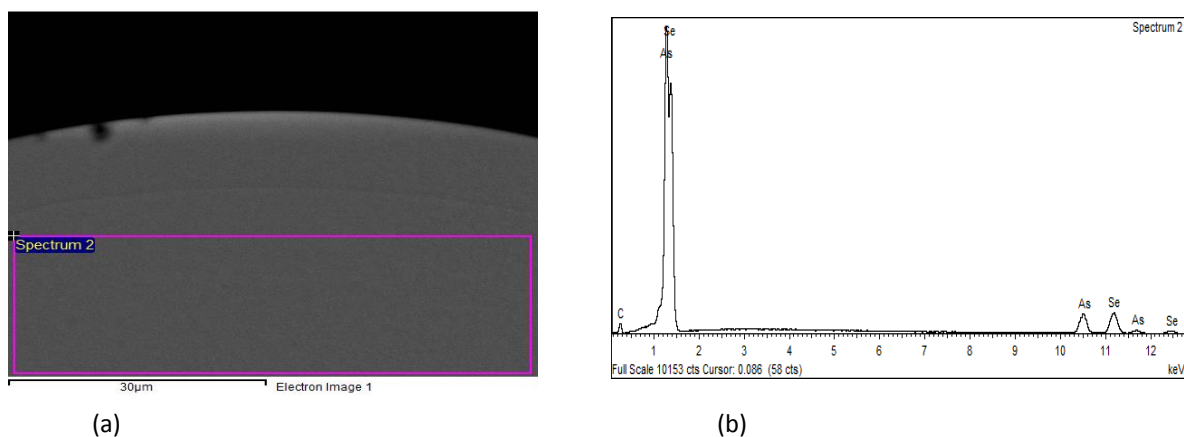


Figure 4.7 F007MINSCGNM fiber large-core step-index fiber: (a) region used to find atomic % of elements and (b) spectrum of elements in the core region.

Table 4.2 F007MINSCGNM fiber large-core step-index fiber: the differences in elemental compositions in **the core region** between the nominal as-batched and measurement.

Element	Nominal batch composition / atomic %	Measured composition / atomic %	% Difference between batch and actual composition
As	40	40.36	+0.9
Se	60	59.64	-0.6

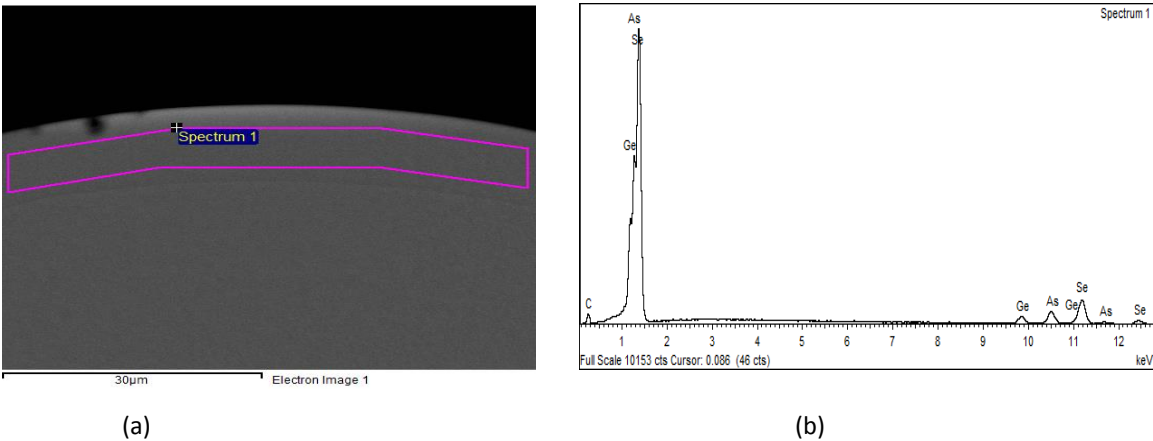


Figure 4.8 F007MINSCGNM fiber large-core step-index fiber: (a) **cladding region** used to find atomic % of elements and (b) spectrum of elements in the **cladding region**.

Table 4.3. F007MINSCGNM fiber large-core step-index fiber: the difference in elemental composition in the cladding between the nominal as-batched composition and the measured.

Element	Nominal batch composition / atomic %	Measured composition / atomic %	Difference between batch and actual composition /atomic %
As	23.4	24.27	0.87
Se	66.6	66.91	0.31
Ge	10	8.82	1.18

4.4.3.2. Results of SEM imaging and analysis of F008MINSCGNM

F008MINSCGNM core/cladding As-Se/Ge-As-Se large-core step-index fiber was cleaved and four sample cross-sections were used for SEM imaging and analysis. Only one sample is shown in all the figures as an example.

SEM images showing the F008MINSCGNM core/cladding = As-Se/Ge-As-Se large-core fiber are in Figs. 4.9 and 4.10.

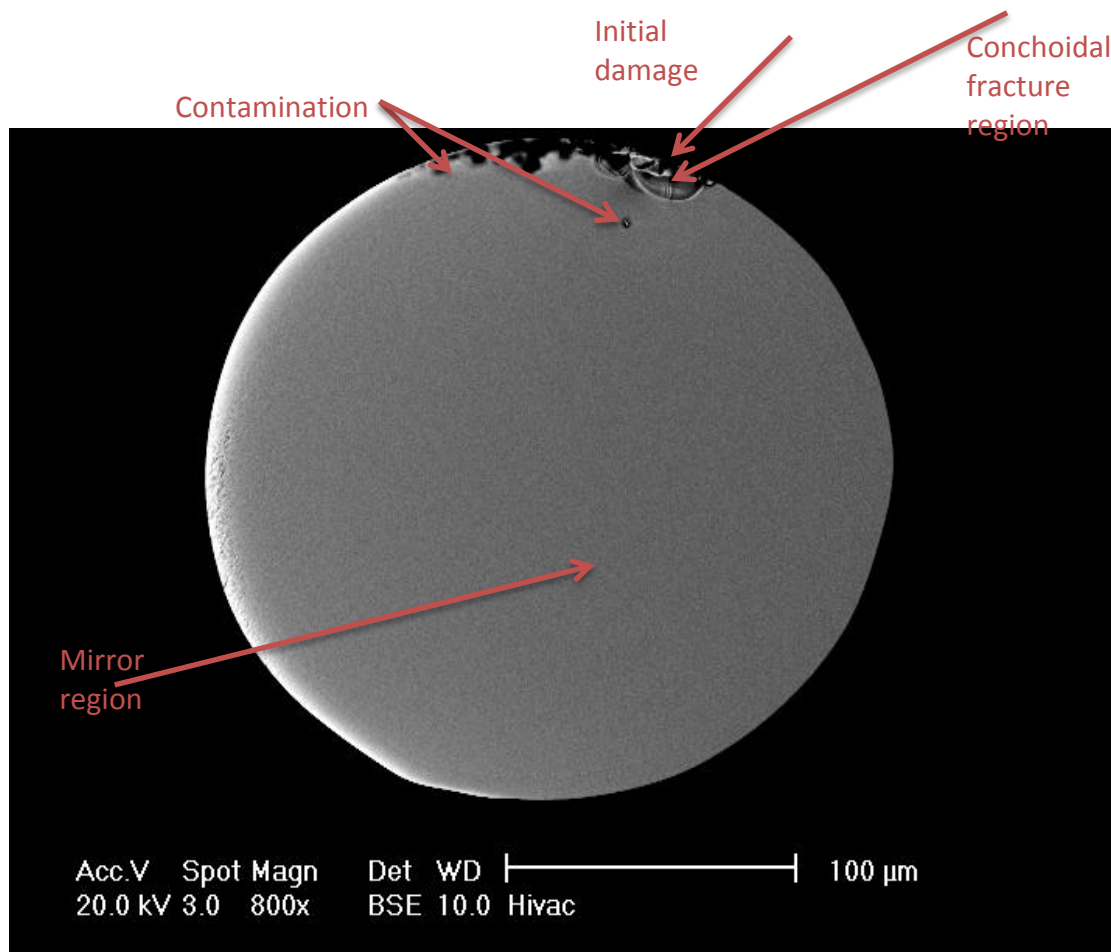


Figure 4.9 SEM imaging of chalcogenide fiber of F008MINSCGNM large-core step-index fiber.

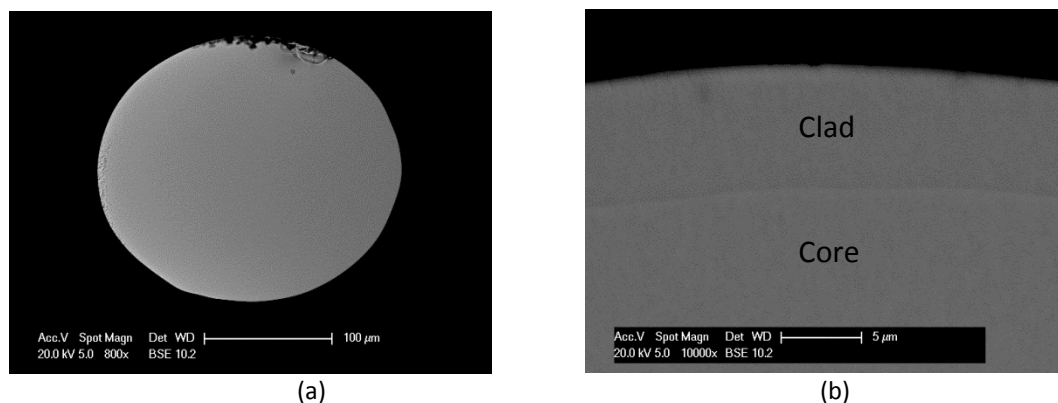


Figure 4.10 F008MINSCGNM large-core step-index fiber: (a) boundary between the core and the cladding and (b) at higher magnification.

The core diameter and OD of the F008MINSCGNM large-core/cladding fiber were measured using SEM. Each diameter was measured two times in a different orientation (see Fig. 4.11) and the average values were calculated to find the core diameter, OD and cladding thickness.

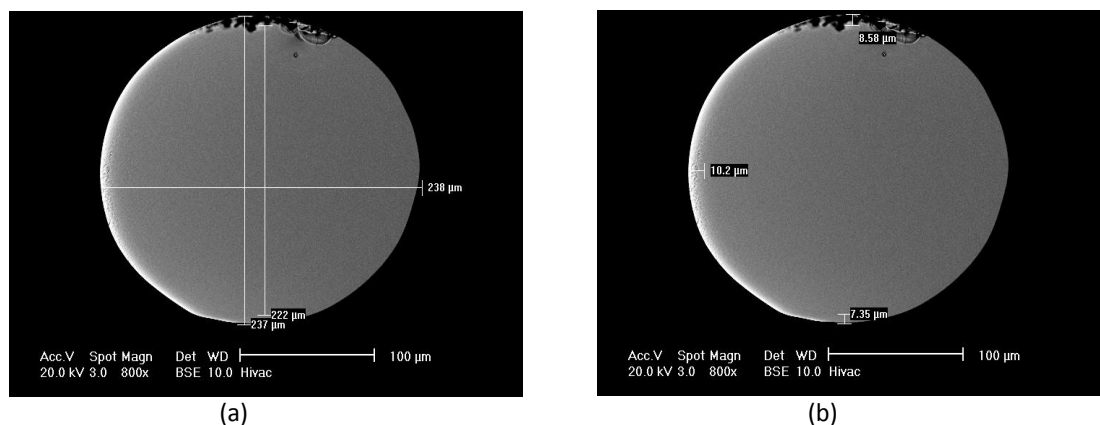


Figure 4.11 F008MINSCGNM large-core step-index fiber: (a) lines for measuring the core diameter and (b) lines for measuring the average OD.

Table 4.4. F008MINSCGNM large-core step-index fiber: the average and standard deviation dimensions of six samples of F008MINSCGNM fiber.

Fiber sample	Average OD / μm	Average core diameter/ μm	Average cladding thickness / μm
1	237.0 ± 4	222.0 ± 0	8.2 ± 1.1
2	237.5 ± 0.5	222.0 ± 0	8.7 ± 1.0
3	222.5 ± 2.5	207.0 ± 2	8.2 ± 0.4
4	222.5 ± 4.5	207.0 ± 4	9.2 ± 0.9

Due to the physical damage problem, which made the SEM imaging rather ambiguous, the % asymmetry was not calculated for the F008MINSCGNM fiber.

SEM-EDS elemental mapping of the F008MINSCGNM fiber large-core step-index fiber showed three elements were present: As, Ge and Se. As and Se were depleted in the cladding and Ge was only present in the cladding, as expected (Fig. 4.12). The elemental composition of both the core and cladding compositions in the F008MINSCGNM fiber were within 1.63 atomic % absolute of the nominal as-batched compositions (see Figs. 4.13 and 4.14, and Tables 4.5 and 4.6).

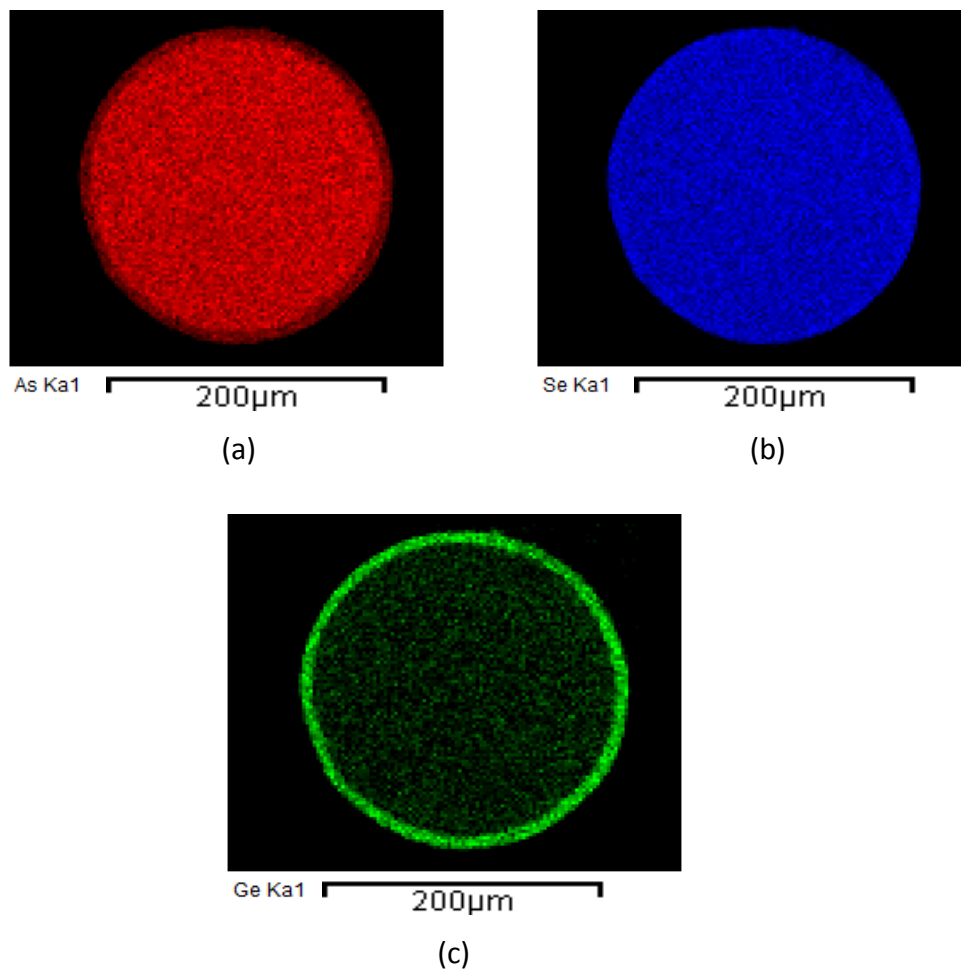


Figure 4.12 F008MINSCGNM large-core step-index fiber, elemental mapping: (a) As; (b) Se and (c) Ge.

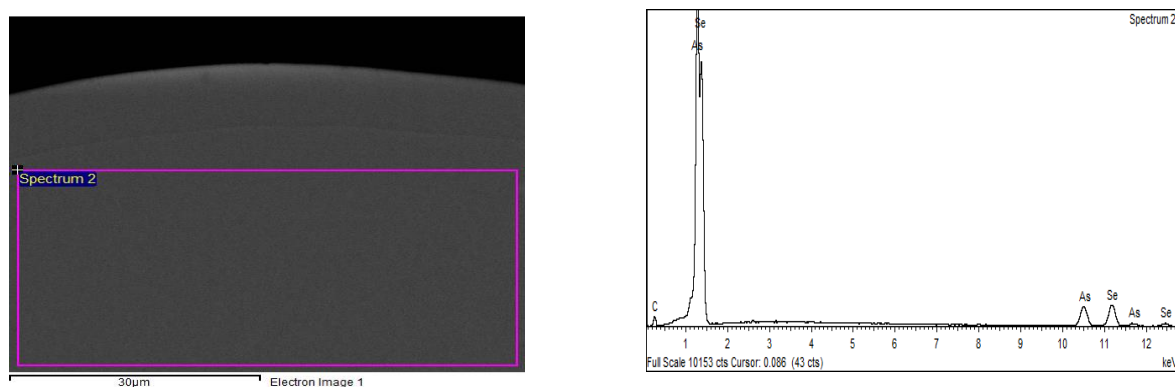


Figure 4.13 F008MINSCGNM large-core step-index fiber: (a) region used to find atomic % of elements and (b) spectrum of elements in the core region.

Table 4.5. F008MINSCGNM large-core step-index fiber: the difference in elemental composition in the core between the nominal as-batched and measured.

Element	Nominal batch composition / atomic %	Measured composition / atomic %	Difference between batch and actual composition / atomic %
As	40	40.64	0.64
Se	60	59.36	1.07

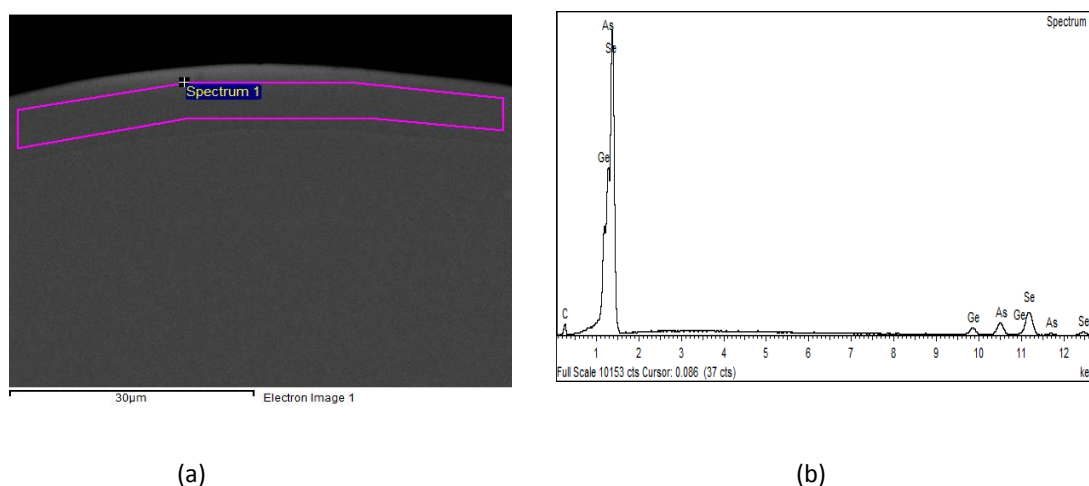


Figure 4.14 F008MINSCGNM large-core step-index fiber: (a) region used to find atomic % of elements and (b) spectrum of elements in the cladding region.

Table 4.6 F008MINSCGNM large-core step-index fiber: the difference in elemental composition of the cladding glass between the nominal as-batched and measured.

Element	Nominal batch composition / atomic %	Measured composition / atomic %	Difference between batch and actual composition / atomic %
As	23.4	25.19	+ 0.79
Se	66.6	66.44	- 0.16
Ge	10.0	8.37	- 1.63

4.4.3.3. Results of far field imaging of F007MINSCGNM and F008MINSCGNM

The far field imaging results are shown for F007MINSCGNM (see Figs. 4.15(a) to (d)) and F008MINSCGNM (see Figs. 4.16 (a) to (d)). Note that during the far-field imaging experiments, the angle of input of the source light was deliberately altered in the case of the result shown in the plot in Fig. 15 (d) compared to the plots in Fig. 15 (a) to (c) for F007MINSCGNM fiber, for which the angle of input of the source light was the same, and same is true of the plot in Fig. 16 (d) compared to the plots in (a) to (c) of Fig. 16 for the

F008MINSCGNM fiber. All of the plots showed a smooth decrease in light intensity with increase in angle from the maximum light intensity at the 0°, normal position.

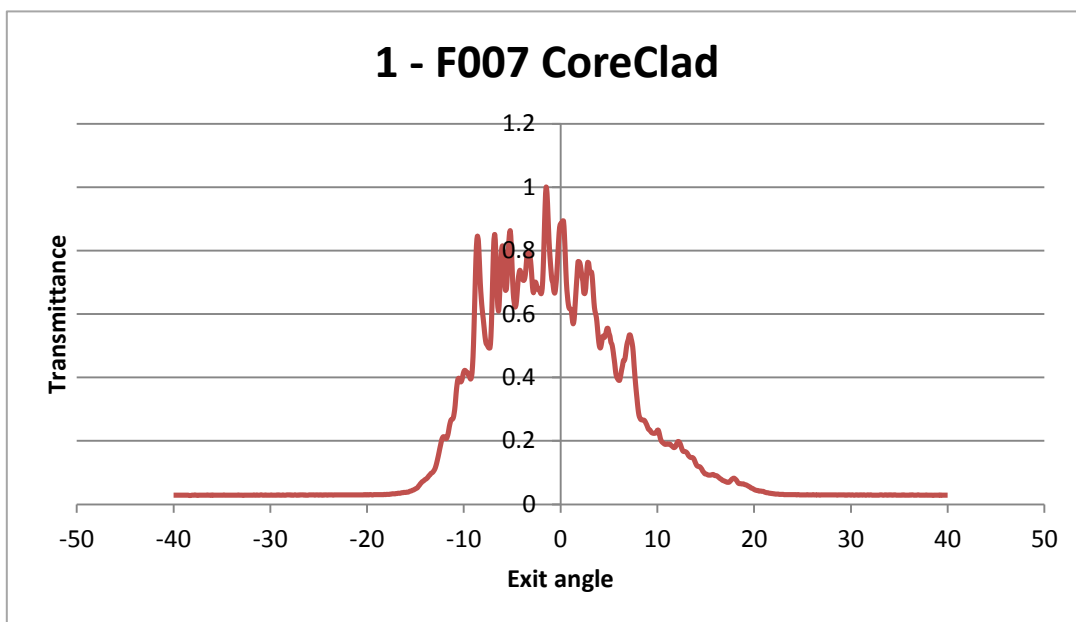


Figure 4.15(a) The intensity of the exit light with different angle of the F007MINSCGNM fiber.

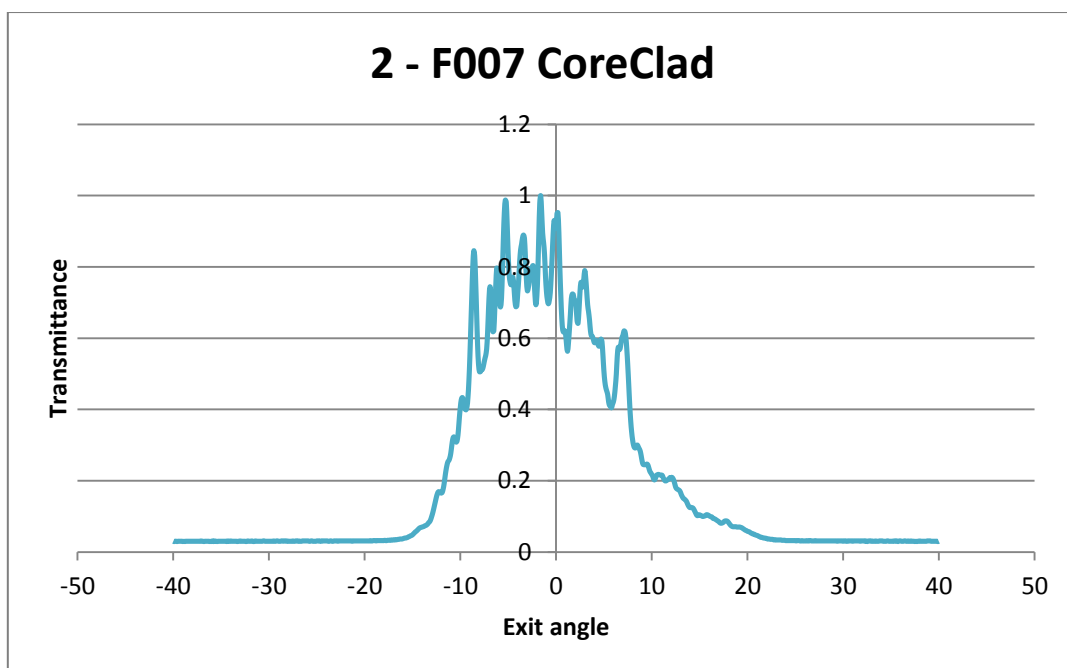


Figure 15(b). The intensity of the exit light with different angle of the F007MINSCGNM fiber.

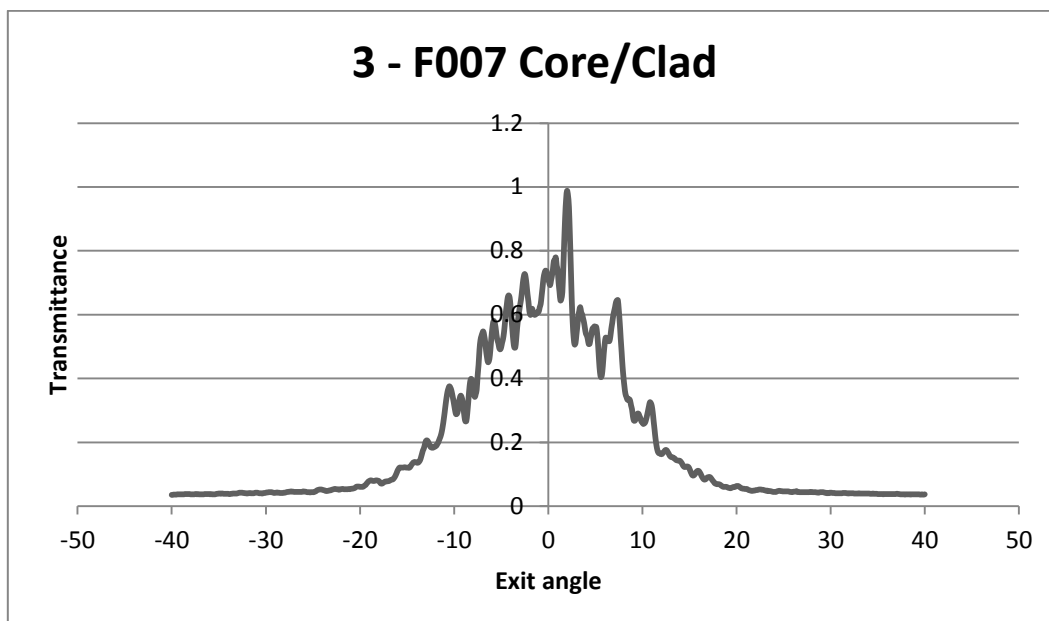


Figure 15(c). The intensity of the exit light with different angle of the F007MINSCGNM fiber.

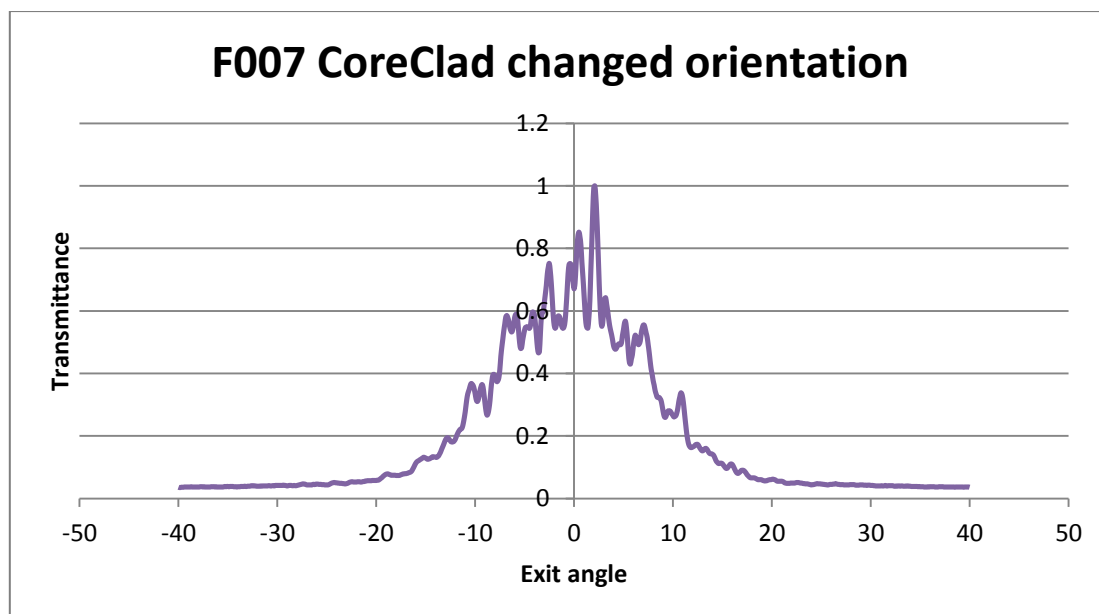


Figure 4.15(d). The intensity of the exit light with different angle of the F007MINSCGNM fiber.

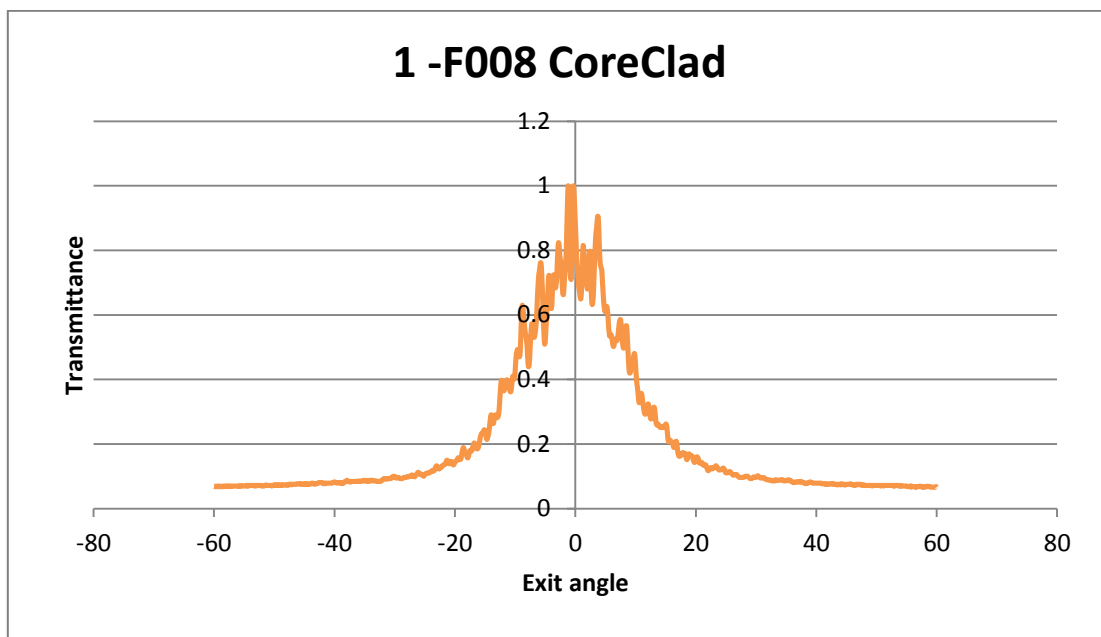


Figure 4.16(a). The intensity of the exit light with different angle of the F008MINSCGM fiber.

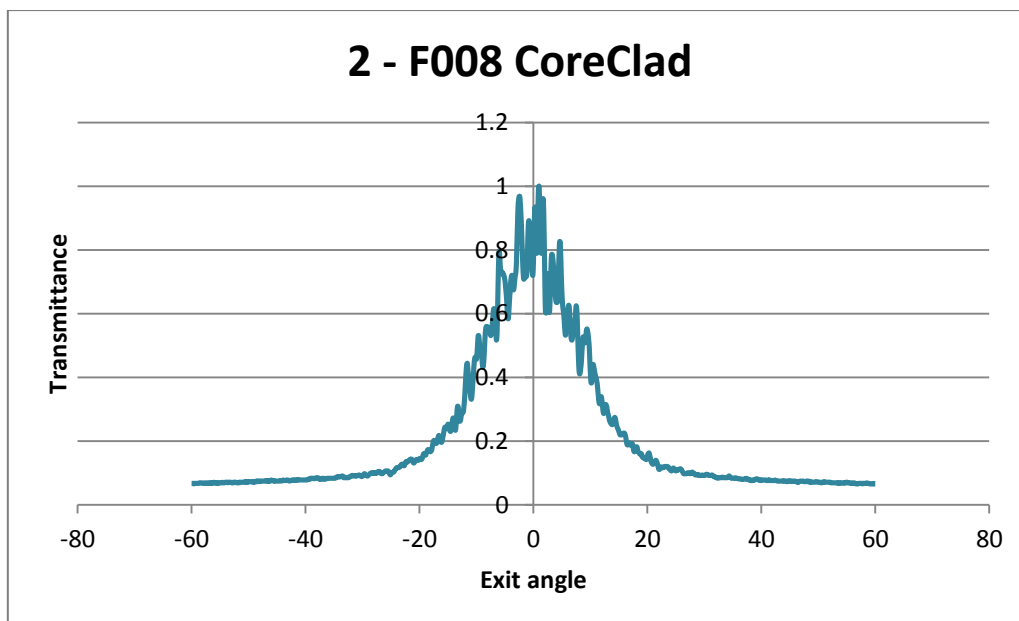


Figure 4.16(b). The intensity of the exit light with different angle of the F008MINSCGM fiber.

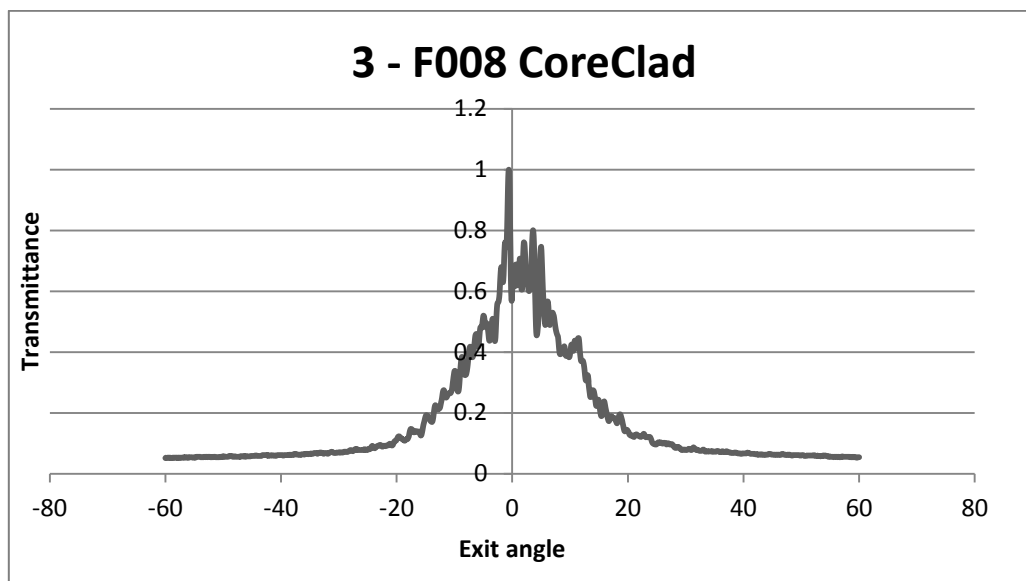


Figure 4.16(c). The intensity of the exit light with different angle of the F008MINSCGNM fiber.

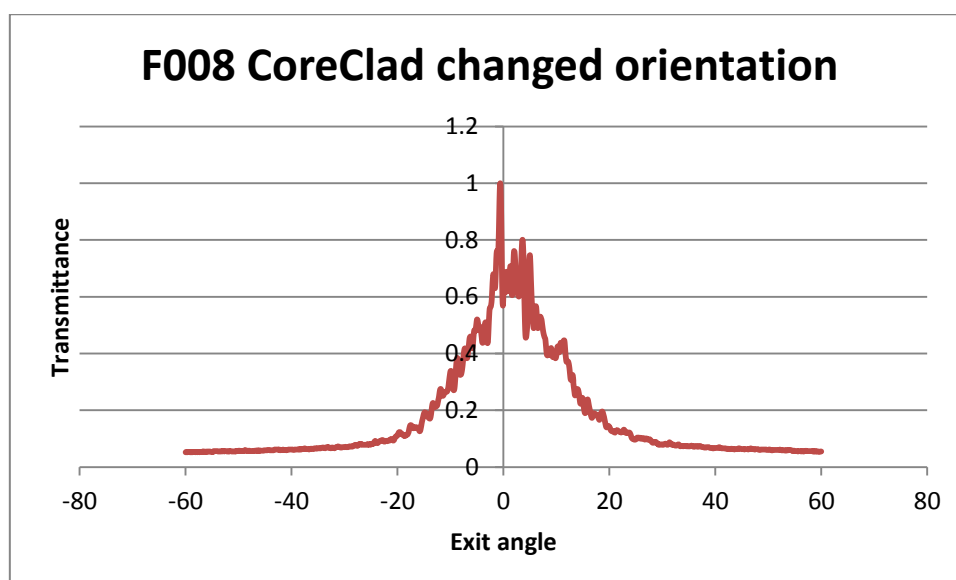


Figure 4.16(d). The intensity of the exit light with different angle of the F008MINSCGNM fiber.

4.4.3.4 Collation of SEM-EDS and far field imaging results of F007MINSCGNM and F008MINSCGNM and discussion

Table 4.7 is a collation of the SEM-EDS measured elemental compositions of the F007MINSCGNM and F008MINSCGNM fibers compared to the nominal batch compositions of the glasses melted to make up the core and cladding glasses of which these fibers comprise. Results for a third fiber: F003MINSCGNM, are included in Table 4.7.

At the University of Nottingham, UK, it is well known that this type of SEM-EDS analytical measurement can only be made within a precision of $\pm 0.5\%$. Hence, it can be concluded that the measurements indicate that the measured elemental compositions for the As-Se binary glasses making up the core glass of each fiber are extremely close to those nominally batched and within the errors of the measurement itself. On the

other hand, for the Ge-As-Se glasses, the Ge content is a little low and at worst 1.6 atomic % lower than that nominally batched and hence during the glass melting some of the germanium content must be lost. This feature appears to be reproducible throughout the three different fibers: F007MINSCGNM, F008MINSCGNM and F003MINSCGNM.

Table 4.7 Collation of mean SEM-EDS atomic% analysis of MIR- transmitting selenide-chalcogenide fibers.

	Element	Nominal batch composition	F003MINSCGNM	F007MIN-SCGNM	F008MIN-SCGNM
Core glass	As	40	39.75	40.36	40.64
	Se	60	60.25	59.46	59.36
Cladding glass	Ge	10	8.66	8.82	8.37
	As	23.4	25.02	24.28	25.19
	Se	66.6	66.31	66.91	66.44

The dependence of the light-intensity from the MIR-transmitting selenide-chalcogenide optical fiber on exit-angle, and hence the fiber NA, were measured for fibers F007MINSCGNM and F008MINSCGNM. As noted above, the light intensity was maximum in each case at an exit angle of 0° and fell as the angle of measurement of the light exiting the fibers increased. However, the maximum angle in each case was $\pm 20^\circ$. Using the equation:

$$NA = \sin \theta \quad (4.1)$$

where θ is half of the solid angle of acceptance of light, or emergence of light into, or out of, the fiber respectively. The resulting calculated NA for each sample were found to be 0.09 at 980 nm for both of the silica-glass based fibers (please see Section 3 of this Report) and 0.17 at 1.54 μm wavelength for all of the selenide-chalcogenide fibers measured; these NAs are collated in Table 4.2.

Table 4. 8. Collated measurements of NA of silica-glass fibers (please see Section 3) at 980 nm and of MIR-transmitting selenide-chalcogenide optical fiber at 1.54 nm.

Fiber type	Standard Telecom silica-glass fiber	Multimode Telecom silica-glass fiber	P020 As-Se	F018 GeSbSe	F007MIN-SCGNM	F008MIN-SCGNM
Measured NA	0.09	0.09	0.17	0.17	0.17	0.17
Calculated NA	Assumed~ 0.3	?	?	?	0.99	0.99

As shown in Table 4.8, the expected NA of the fibers F007MINSCGNM and F008MINSCGNM was 0.99. This is known from previous measurements of the refractive index dispersion of these core and cladding glasses using MIR ellipsometry, see references [4.2, 4.3] and calculation of the NA. Not only that, the far field measurements of fiber NA appeared to be invariant of fiber composition.

By studying briefly the theory of Fresnel reflection, Brewster angle and critical angle (please see Section 4 Appendix I), it could be concluded that these constraints at the end of the chalcogenide fiber do not totally influence the NA and variation of light-intensity with exit angle of the chalcogenide fiber.

It is now realised that the measured NA was actually an artefact of the way that the measurements were carried out. What was measured in each case was the étendue of the laser source, itself, because the NA of the laser source was smaller than that of the fibers being measured; hence the laser source had not filled all possible mode paths inside the fiber.

Future measurements will be arranged such that there is a high NA lens in front of the laser source of higher NA than the expected NA of the fiber to be measured. This will be tricky in the case of the high NA selenide chalcogenide fibers and a germanium or of tellurium-based chalcogenide glass spherical lens may be required. Another idea is to lens the end of the fiber itself. Other considerations are the need to cladding mode-strip the fiber length immediately beyond the fiber input-face.

4.5 Near-field rig

Our in-house near-field rig equipped with a near-infrared (NIR) camera and, using this, we have measured imaged NIR light guiding in both large-core and small-core selenide-chalcogenide step index fiber (SIF) using the following method.

4.5.1 Methodology

Near-field, NIR imaging of 55-60 mm long samples has been *via* a tunable laser: 1.465 – 1.575 μm (Agilent; 8164B). NIR light was launched into the using a tapered silica-fiber, mounted on a XYZ translation stage, with focused spot size 2.5 μm at the chalcogenide SIF launch-end. The output light was collected using a microscope x10 objective and collimated onto a Siemens XQ1112 vidicon tube camera.

4.5.2 Typical results

Table 6.1 gives a summary of all of the Ge-Sb-Se fibers checked for near-field imaging and their properties; refractive indices were taken from [4.4]. Fig. 4.17 shows typical near-field images collected at 1463 nm wavelength. The 1463 nm laser light was launched into 500 \pm 1.5 mm lengths of cleaved fiber, using an objective x10 microscope lens. Fibers are listed in Table 4.9 and were: F019JHB (glass pair I) with intended core sizes: (a) 15 μm ; (b) 10 μm and (c) 7 μm ; F023JHB (glass pair II) with intended core sizes: (d) 15 μm ; (e) 10 μm and (f) 7 μm and F035JHB (glass pair III) with intended core sizes: (g) 15 μm and (h) 10 μm . The results confirm light confinement within the central core region. Scale bar given in (a) applies to all images. See Table 4.9 for the core/cladding composition and measured core dimensions of each fiber type. Note that F032JHB did not light guide.

Table 4.9. Summary of the Ge-Sb-Se fibers checked for near-field imaging at 1463 nm and their properties. Refractive indices were taken from [4.5]. Key: - means it did not guide. See Fig. 4.17.

Fibre code	Glass pair	Core composition / (at. %)	Cladding composition / (at. %)	Predicted core ϕ / (μm)	Measured core dimensions from SEM images in Chapter 5 / (μm)	Refractive index of core at 1463 nm	Refractive index of cladding at 1463 nm	Near-field light guiding image in Figure 6.1
F019JHB	Pair I	$\text{Ge}_{22}\text{Sb}_8\text{Se}_{70}$	$\text{Ge}_{24}\text{Sb}_4\text{Se}_{72}$	15	20.30 x 9.08	2.549 ± 0.002	2.491 ± 0.003	(a)
				10	12.70 x 5.52			(b)
				7	10.50 x 4.81			(c)
F023JHB	Pair I	$\text{Ge}_{22}\text{Sb}_8\text{Se}_{70}$	$\text{Ge}_{24}\text{Sb}_4\text{Se}_{72}$	15	20.40 x 10.10	2.549 ± 0.002	2.491 ± 0.003	(d)
				10	13.0 x 7.70			(e)
				7	9.48 x 4.69			(f)
F032JHB	Pair II	$\text{Ge}_{19}\text{Sb}_{15}\text{Se}_{66}$	$\text{Ge}_{20}\text{Sb}_{10}\text{Se}_{70}$	15	16.40 x 12.10	2.676 ± 0.003	2.576 ± 0.003	-
				10	9.47 x 7.11			-
F035JHB	Pair III	$\text{Ge}_{20}\text{Sb}_{10}\text{Se}_{70}$	$\text{Ge}_{24}\text{Sb}_4\text{Se}_{72}$	15	14.32 x 12.70	2.576 ± 0.003	2.491 ± 0.003	(e)
				10	~16*			(f)

*the core was difficult to distinguish from SEM images but was detected from EDX analysis.

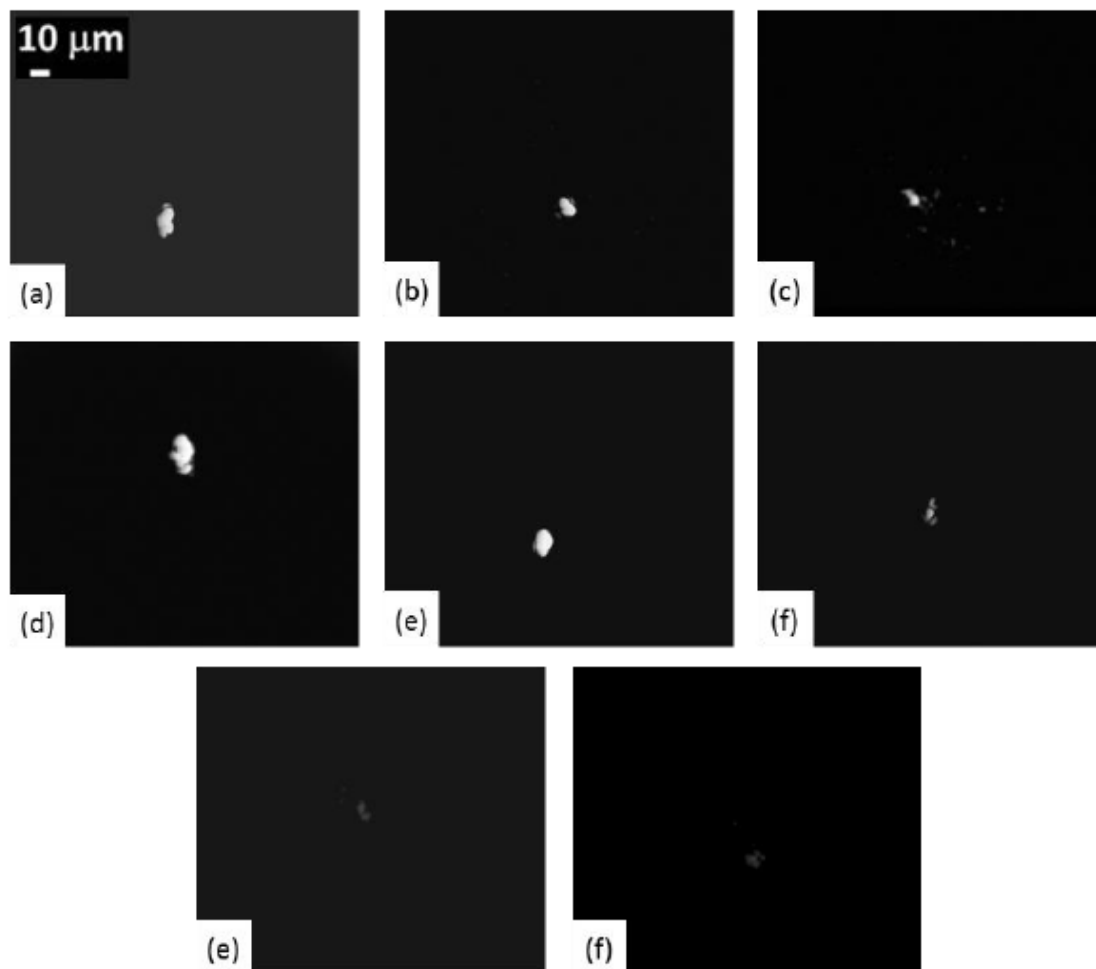


Figure 4.17 Near-field images of light at 1463 nm wavelength, using a B1980A tunable diode laser. 980 nm wavelength / 15 mW was launched into 500 ± 1.5 mm cleaved fiber using an objective x10 microscope lens. Fibers were: F019JHB (glass pair I) with intended core sizes: (a) 15 μm ; (b) 10 μm and (c) 7 μm ; F023JHB (glass pair II) with intended core sizes: (d) 15 μm ; (e) 10 μm and (f) 7 μm and F035JHB (glass pair III) with intended core sizes: (g) 15 μm and (h) 10 μm . The results confirm light confinement within the central core region. Scale bar given in (a) applies to all images. See Table 4.9 for the core/cladding composition and measured core dimensions. Note that F032JHB did not light guide. (Images are from [4.4]).

4.6 Novel resonant pumping using the MIR-QCL

We report here our work on novel resonant pumping of rare earth ion doped selenide-chalcogenide fibre. In brief, the experiment was to pump Pr^{3+} doped GeGaAsSe optical fiber using the new MIR-QCL at ~ 4 μm wavelength. For the first time we were able to study excited state absorption by monitoring emission at 2.4 μm wavelength, please see reference [4.1].

This work was published in Jan. 2017 [4.1]; the abstract and conclusions are reproduced below (sections 4.6.1. and 4.6.2). The paper itself is reproduced in Section 4 Appendix I.

We do apologize deeply to EOARD for not acknowledging in this paper their partial funding of the MIR QCL. We will in all future publications duly acknowledge our indebtedness to EOARD for this financial support, for which we are most grateful.

4.6.1 Abstract and conclusions of published paper [4.1]

4.6.1.1 Abstract

Numerical modelling of a Pr^{3+} -doped chalcogenide glass fibre laser is presented in this paper. The spectroscopic parameters are extracted from in-house prepared Pr^{3+} doped selenide-chalcogenide glass samples and used in the modelling. In this contribution, particular attention is paid to a novel resonant pumping scheme. The modelled laser performance is tested as a function of pump wavelength, fibre length, signal wavelength, fibre background loss and output coupler reflectivity. The modelling results show that the proposed resonant pumping scheme, which might be achieved in practice using a high power QCL pump, allows for a significant reduction in the laser threshold and an increase in the laser efficiency. A slope efficiency of 54 % is calculated when the fibre losses are brought down to 1 dB/m.

4.6.1.1 Conclusions

The performance of resonantly pumped selenide chalcogenide glass fibre lasers doped with Pr^{3+} was comprehensively studied. Particular attention was paid to the role of excited state absorption (ESA), which has not been considered previously in the literature on mid-infrared transitions of Pr^{3+} in selenide chalcogenide glasses. ESA absorption cross section spectra were extracted using McCumber theory. The experimentally extracted parameters formed the basis for the numerical model used in this study. The numerical results showed that ESA had a major influence on the laser performance and that its effect could be reduced by selecting the pump wavelength so that $\sigma_{\text{GSA}} > \sigma_{\text{ESA}}$. It was also shown that a resonant pumping scheme using a high power QCL is a better solution when compared with the best pumping scheme reported so far. The results obtained showed that resonant pumping allowed for a significant reduction in the laser threshold, and an increase of the laser efficiency. Furthermore, we showed that knowledge of the ESA spectral distribution is indispensable when selecting the optimal wavelength for resonant pumping.

REFERENCES

- 4.1 L Sójka, ZQ Tang, D Furniss, H Sakr, E Bereś-Pawlik, TM Benson, **AB Seddon**, S Sujecki Numerical and experimental investigation of mid-infrared laser action in resonantly pumped Pr^{3+} doped chalcogenide fiber, *Optical & Quantum Electronics* **49** (13) **2017**.
- 4.2 CR Petersen, U Møller, I Kubat, B Zhou, S Dupont, J Ramsay, T Benson, S Sujecki, N Abdel-Moneim, Z Tang, D Furniss, **A Seddon** and O Bang, Mid-infrared supercontinuum covering the 1.4–13.3 μm molecular fingerprint region using ultra-high NA chalcogenide step-index fiber, *NATURE PHOTONICS* 830–834 **2014**. **CITED BY 228**

This article was selected for *NATURE PHOTONICS News and Views* Entering the mid-infrared: The demonstration of chalcogenide fiber-based supercontinuum sources that reach beyond a wavelength of ten micrometres is set to have a major impact on spectroscopy and molecular sensing. Gr Steinmeyer and Julia S. Skibina *NATURE PHOTONICS* | VOL 8 | NOVEMBER 2014 |
- 4.3 HG Dantanarayana, N Abdel-Moneim, Z Tang, L Sojka, S Sujecki, D Furniss, **AB Seddon**, I Kubat, O Bang, and TM Benson, Refractive index dispersion of chalcogenide glasses for ultra-high numerical-aperture fiber for mid-infrared supercontinuum generation. *Optical Materials Express* **4** (7) 1444-1455 **2014**.
- 4.4 L Qingquan, Mid-Infrared Photonics Group, GGIEMR, Faculty of Engineering, University of Nottingham, UK, “Microstructured optical fibers in chalcogenide glass”, MPhil thesis 2013.
- 4.5 J Butterworth, Mid-Infrared Photonics Group, GGIEMR, Faculty of Engineering, University of Nottingham, UK, “Mid-infrared transmitting Ge-Sb-Se chalcogenide glass fibers: for potential use in medical diagnostics”, PhD thesis submitted January 2017.

Section 4. APPENDIX I

Numerical and experimental investigation of mid-infrared laser action in resonantly pumped Pr^{3+} doped chalcogenide fibre

L. Sójka^{1,2}, Z. Tang¹, D. Furniss¹, H. Sakr¹, E. Bereś-Pawlik², A. B. Seddon¹, T. M. Benson¹ and S. Sujecki^{1*}

¹*Mid-Infrared Photonics Group, George Green Institute for Electromagnetics Research, University of Nottingham, University Park, NG7 2RD Nottingham, UK*

²*Telecommunications and Teleinformatics Department, Wrocław University of Technology, Wybrzeże Wyspiańskiego 27, 50-370 Wrocław, Poland*

*slawomir.sujecki@nottingham.ac.uk

Abstract:

Numerical modelling of a Pr^{3+} -doped chalcogenide glass fibre laser is presented in this paper. The spectroscopic parameters are extracted from in-house prepared Pr^{3+} doped selenide-chalcogenide glass samples and used in the modelling. In this contribution, particular attention is paid to a novel resonant pumping scheme. The modelled laser performance is tested as a function of pump wavelength, fibre length, signal wavelength, fibre background loss and output coupler reflectivity. The modelling results show that the proposed resonant pumping scheme, which might be achieved in practice using a high power QCL pump, allows for a significant reduction in the laser threshold and an increase in the laser efficiency. A slope efficiency of 54 % is calculated when the fibre losses are brought down to 1 dB/m.

Key words: mid-infrared fibre laser, chalcogenide glass, mid-infrared, rare earth doped glass

1. Introduction

High power mid-infrared fibre laser sources with emitting wavelengths covering the range stretching from 4 μm to 5.5 μm offer many applications in remote sensing, medicine and defence (Seddon 2011; Seddon 2013; Pollnau and Jackson 2008; Jackson 2012). However, in order to access these wavelengths, low phonon energy host materials are needed. Among the most promising host materials for this wavelength region are chalcogenide glasses (Seddon 2010; Tao et al. 2015). Chalcogenide glasses possess good rare earth ion solubility, high refractive index and can be drawn into fibre. These characteristics make chalcogenide glasses an attractive host material for rare-earth ions (Seddon 2010; Tao et al. 2015). Recent publications show that there is a particularly large interest in mid-infrared fluorescence from the $(^3\text{F}_2, ^3\text{H}_6) \rightarrow ^3\text{H}_5$ ($\sim 3.7\text{--}4.2 \mu\text{m}$), and $^3\text{H}_5 \rightarrow ^3\text{H}_4$ ($4.3\text{--}5.0 \mu\text{m}$) transitions of Pr^{3+} doped selenide glass (Sakr et al. 2014; Sójka et al. 2014; Karaksina et al. 2016; Shpotyuk et al. 2015; Karaksina et al. 2016; Chahal et al. 2016; Shaw et al. 2001). This is because Pr^{3+} ions in chalcogenide glass have a high pump absorption cross-section, and also because Pr^{3+} can be pumped with commercially available laser diodes. Despite this, a Pr^{3+} doped selenide chalcogenide glass fibre laser has not yet been realized. The first problem that stops this technology is the difficulty of manufacturing high purity rare earth doped chalcogenide glasses. Secondly, both the upper and lower laser manifolds possess long lifetimes in comparison to that of the ground state. This tends to cause self-terminating laser operation and makes achieving population inversion difficult. One possible solution to this latter obstacle can be cascading two laser transitions (Quimby et al. 2008). However, the practical realization of cascading is challenging, since it requires the fabrication of two pairs of wavelength-matched fibre gratings in the Pr^{3+} doped chalcogenide glass fibre. Additionally, significant pump power is required in order to achieve laser action for both transitions. Thus, a potentially better solution is to pump the laser resonantly using a QCL (quantum cascade laser). The low quantum defect of the resonantly pumped praseodymium ions potentially enables the fibre laser to achieve high wall-plug efficiency. Further,

the resonant pumping reduces the thermal load due to a low quantum defect. This feature is particularly important for fibres fabricated from low glass transition temperatures like chalcogenide glasses. Currently, high power QCLs operating around 4.1 μm are commercially available (<http://www.pranalytica.com>; Rauter et al. 2013). Resonant pumping of the Pr^{3+} ions in low phonon laser crystals using QCLs was suggested in (Ferrier et al. 2009). However, in that study excited state absorption (ESA) was not included in the model which, as the authors themselves note, is a significant shortcoming.

In this contribution, we therefore have paid particular attention to the ESA processes, the inclusion of which is, as we show, essential for predictive modelling. Hence, we extract the ESA spectrum of the $^3\text{H}_5 \rightarrow (^3\text{F}_2, ^3\text{H}_6)$ transition. Then using a complete set of experimentally extracted modelling parameters, including ESA emission and absorption cross-sections, we developed a numerical model of a resonantly pumped Pr^{3+} selenide fibre laser. Using the model, we study the influence of the ESA on the Pr^{3+} selenide fibre laser performance and identify the best pumping wavelength for obtaining mid-infrared lasing in a resonantly pumped Pr^{3+} , doped selenide chalcogenide glass fibre laser. Finally, we comprehensively study the laser performance as a function of pump wavelength, fibre length, signal wavelength, fibre background loss, and output coupler reflectivity.

The paper is divided into five sections. After this introduction, section 2 describes the experimental results, which confirm the presence of ESA when pumping resonantly. The procedure used to calculate the ESA cross-section is presented in section 3. In section 4, we develop a numerical model of the resonantly pumped Pr^{3+} doped chalcogenide glass fibre laser and perform a numerical study of the resonantly pumped fibre laser characteristics. Finally, some conclusions are drawn in section 5.

2. Experimental proof of the presence of ESA

A schematic diagram of the Pr^{3+} energy level structure in a selenide glass host, and relevant transitions, when pumping with a QCL, are presented in Fig.1. The details about chalcogenide glass and fibre fabrication are described elsewhere (Sakr et al. 2014; Sójka et al. 2014; Sójka et al. 2012; Sujecki et al. 2015; Tang et al. 2015). The ESA describes the absorption from a populated excited state of a system to a higher energy state (Kozak et al. 2006; Gomes et al. 2010; Koepke et al. 1998; Caspary 2003; Quimby and Aitken 2003). In this section, the experimental measurements that were carried out in order to prove the presence of ESA are described. The basic experimental setup for ESA measurement is shown in Fig.2. The measurements were carried out within the 1.8 μm – 2.6 μm spectral range. The detection system consisted of a lock-in amplifier (Model 7270, Signal recovery) room temperature extended InGaAs detector with preamplifier (PDA10D-EC, Thorlabs), a data acquisition card (NI USB-6008 National Instruments) and a computer. The monochromator and data acquisition systems were controlled using in-house developed software based on LabView. A 115 mm long unstructured fibre, of 250 μm diameter, was used in the experiment. A mid-infrared pump at 4.15 μm from a QCL (Model 1101-4150-CW-1500, Pranalytica) was launched into one end of the Pr^{3+} doped selenide fibre using a Black Diamond lens of focal length $f = 5.95$ mm. The photoluminescence was collected from the opposite fibre end.

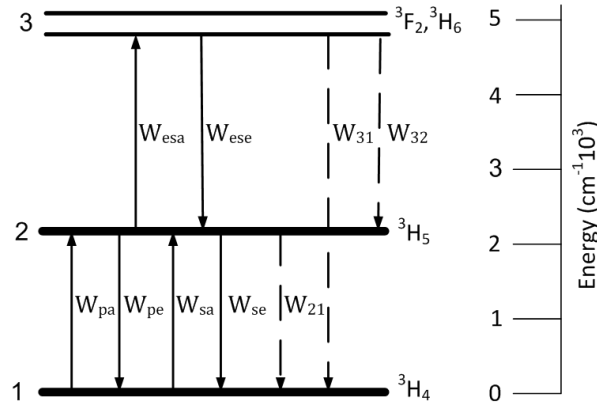


Fig.1. Simplified energy level diagram of Pr^{3+} in a selenide chalcogenide glass host. The ${}^3\text{H}_5$ level can be populated using optical pumping at a wavelength around $4.15\ \mu\text{m}$. The ESA from ${}^3\text{H}_5$ to the (${}^3\text{F}_2, {}^3\text{H}_6$) level is indicated (W_{esa}). The transition rates depicted in Fig.1 are defined as follows: the absorption and emission rates W_{pa} , W_{pe} , W_{sa} , W_{se} of the pump and signal, respectively, W_{esa} the ESA of the pump from ${}^3\text{H}_5 \rightarrow ({}^3\text{F}_2, {}^3\text{H}_6)$, W_{ese} the emission of the pump from $({}^3\text{F}_2, {}^3\text{H}_6) \rightarrow {}^3\text{H}_5$, $W_3 = W_{31} + W_{32}$ the spontaneous decay rate of level 3, W_{21} the spontaneous decay rate of level 2.

The presence of the ESA process was proven in the Pr^{3+} doped selenide fibre by observation of emission centred at a wavelength of $2.4\ \mu\text{m}$, from the level $({}^3\text{F}_2, {}^3\text{H}_6) \rightarrow {}^3\text{H}_4$, whilst pumping at a wavelength of $4.15\ \mu\text{m}$. The measured shape of the $2.4\ \mu\text{m}$ emission is shown in Fig. 3. Therefore the observed emission at around $2.4\ \mu\text{m}$ from the level $({}^3\text{F}_2, {}^3\text{H}_6) \rightarrow {}^3\text{H}_4$ demonstrates that level $({}^3\text{F}_2, {}^3\text{H}_6)$ is populated by the $4.15\ \mu\text{m}$ pump. The photoluminescence shape at $2.4\ \mu\text{m}$ was measured from the fibre end opposite to the launch end, thus it can be affected by photon trapping (diffusion) and reabsorption. A $115\ \text{mm}$ long fibre was used in the experiment. Additionally, a sharp cut-off of the spectrum for wavelengths above $2.5\ \mu\text{m}$ can be attributed to the extended InGaAs detector cut-off. These results directly confirm ESA in the Pr^{3+} doped selenide fibre when pumped at $4.15\ \mu\text{m}$. Therefore, the ESA should be included in the laser model. To the best of our knowledge this is the first time that experimental evidence has been presented for ESA in a Pr^{3+} doped selenide fibre whilst resonant pumping at around $4\ \mu\text{m}$.

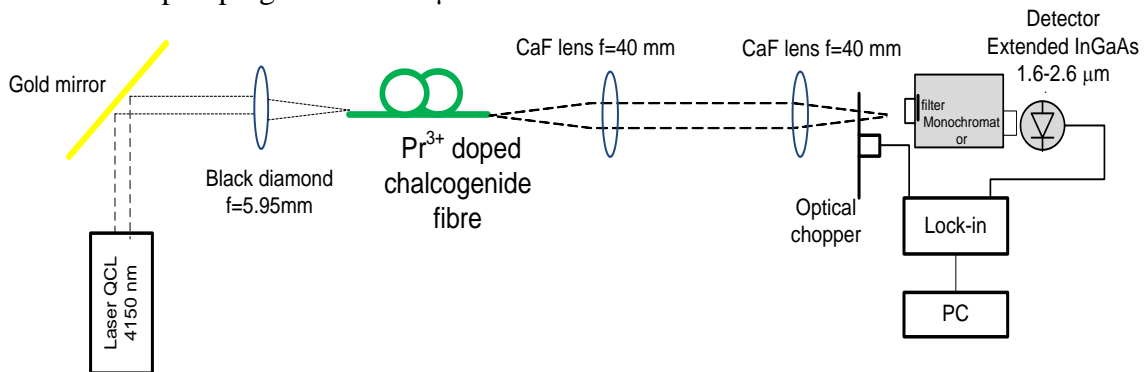


Fig.2.

Experimental setup used for ESA measurement.

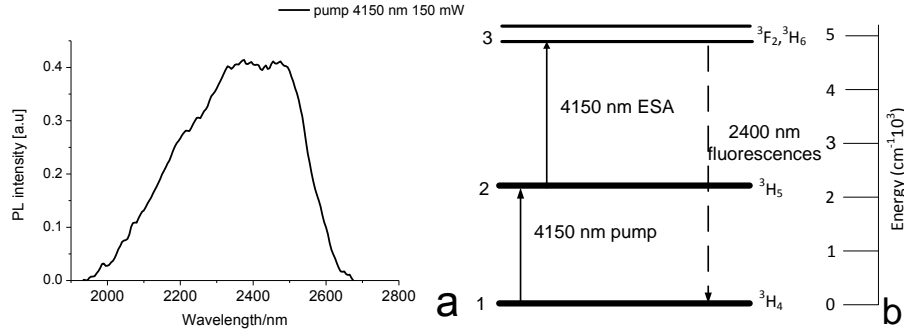


Fig. 3. a) Emission spectrum from ($^3F_2, ^3H_5$) \rightarrow 3H_4 when Pr^{3+} -doped selenide fibre is pumped at a wavelength around 4.15 μm confirming the presence of ESA and b) shows simplified energy level diagram of Pr^{3+} in a selenide chalcogenide glass host. The 2.4 μm fluorescence is indicated by the dashed line.

3. Calculation of ESA cross section

To evaluate numerically the effect of the ESA on the laser efficiency of the Pr^{3+} doped selenide fibre, the absorption cross-section related to the $^3H_5 \rightarrow (^3F_2, ^3H_6)$ transition must be known. In this contribution, we estimated the ESA cross-sections using the Judd-Ofelt (J-O) theory, the McCumber method, and the Fuchtbauer-Ladenburg (F-L) equation (Gomes et al. 2010). The rates of spontaneous emission for ($^3F_2, ^3H_6$) \rightarrow 3H_5 , and $^3H_5 \rightarrow ^3H_4$ transitions were calculated using our Judd-Ofelt parameters for Pr^{3+} doped selenide glass: $\Omega_2=8.156$, $\Omega_4=8.08$, $\Omega_6=5.70$, which were recalculated after removing Se-H contribution at 4.5 μm from absorption spectra. Taking into consideration the small energy difference between the levels 3F_2 and 3H_6 it may be assumed that both levels are in thermal equilibrium. Thus, using Boltzmann statistics, the total radiative rate from the combined pair of levels is given by (Casparly 2003; Quimby and Aitken 2003).

$$A_r = \frac{13A_1 + 5 \cdot A_2 \cdot e^{-\left(\frac{\Delta E}{kT}\right)}}{13 + 5e^{-\left(\frac{\Delta E}{kT}\right)}} \quad (1)$$

where $A_1=273 s^{-1}$ and $A_2=2270.4 s^{-1}$ are the Judd-Ofelt calculated rates from levels 3F_2 (5-fold degenerate level) and 3H_6 (13-fold degenerate level) and ΔE is the spacing between the levels. $\Delta E=600 cm^{-1}$ was used in the calculations (Shaw et al. 2001). Values of radiative rates (electronic (A_{ed}), and magnetic (A_{md}) dipole contribution) and radiative branching ratios obtained from J-O calculations for other transitions in Pr^{3+} selenide chalcogenide bulk glass are listed in Table 1. Calculated radiative lifetimes, non-radiative lifetimes and total lifetimes for the ($^3F_2, ^3H_6$) \rightarrow 3H_5 and $^3H_5 \rightarrow ^3H_4$ transitions are given in Table 2. The multi-phonon non-radiative lifetimes were estimated based upon the data presented in (Shaw et al. 2001). The total fluorescence lifetime is given by a sum of radiative and non-radiative lifetimes. The total fluorescence lifetime is calculated using the following formula:

$$\frac{1}{\tau_{tot}} = \frac{1}{\tau_{rad}} + \frac{1}{\tau_{nr}} \quad (2)$$

where τ_{rad} and τ_{nr} are radiative and non-radiative lifetimes, respectively.

According to the results presented in Table 1 and Table 2, the ($^3F_2, ^3H_6$) \rightarrow 3H_5 , and $^3H_5 \rightarrow ^3H_4$ transitions have a similar strength. Thus, for 2 μm pumping, these transitions are self-terminating. This causes population bottlenecking as a result of the comparatively long lifetime of the ($^3F_2, ^3H_6$) \rightarrow 3H_5 transition, and saturation of the laser output. The calculated ESA absorption cross-section is presented in Fig.3. The maximum cross-section for ESA is equal to $1.23 \times 10^{-24} m^2$ at $\lambda=3.76 \mu m$.

Table 1. Radiative rates (electronic (A_{ed}), and magnetic (A_{md}) dipole contribution) and radiative branching ratios (β) for $^3F_2 \rightarrow ^3H_6$, $^3F_2 \rightarrow ^3H_5$, $^3H_6 \rightarrow ^3H_5$, $^3F_2 \rightarrow ^3H_4$, $^3H_6 \rightarrow ^3H_4$ and $^3H_5 \rightarrow ^3H_4$ transitions in Pr^{3+} selenide chalcogenide bulk glass as calculated using Judd-Ofelt theory.

Transition	$A_{ed}/(s^{-1})$	$A_{md}/(s^{-1})$	β
$^3F_2 \rightarrow ^3H_6$	1.97		6.29e-4
$^3F_2 \rightarrow ^3H_5$	370.2		0.118
$^3F_2 \rightarrow ^3H_4$	2759.2		0.881
$^3H_6 \rightarrow ^3H_5$	72.76	2.14	0.44
$^3H_6 \rightarrow ^3H_4$	91.81		0.56
$^3H_5 \rightarrow ^3H_4$	79.50	1.85	1

Table 2. Calculated radiative lifetimes (τ_{rad}), non-radiative lifetime (τ_{nr}) (multi-phonon relaxations) and total lifetimes (τ_{tot}). The non-radiative lifetimes are estimated upon results presented in (Shaw et al. 2001)

Transition	Calculated radiative lifetime τ_{rad} /(ms)	Estimated non-radiative lifetime τ_{nr} /(ms)	Calculated total lifetime τ_{tot} /(ms)	τ_{tot}/β /(ms)
$(^3F_2, ^3H_6) \rightarrow ^3H_5$	4.56	322.6	4.49	10.2
$^3H_5 \rightarrow ^3H_4$	12.2	60.0	10.0	10.0

ESA cross section was derived using McCumber theory and based on the emission spectrum for the $(^3F_2, ^3H_6) \rightarrow ^3H_5$ transition that has been reported in (Shaw et al. 2001) and scaled by us using the Fuchtbauer-Ladenburg equation to match the spontaneous emission rate for the $(^3F_2, ^3H_6) \rightarrow ^3H_5$ transition. This method of extracting ESA from emission measurements using McCumber theory was described by Quimby and Zheng in (Quimby, and Zheng 1992). The result of this calculation is shown in Fig.4a. In Fig.4b we present both the absorption and emission cross sections of this ESA. Fig 4b shows the characteristic redshift between absorption and emission cross section, which agrees with expectations (Quimby, and Zheng 1992).

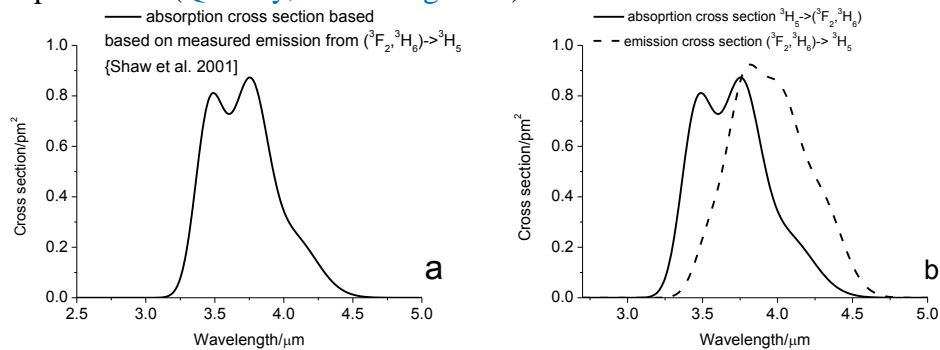


Fig.4 a) ESA cross-section calculated for the transition $^3H_5 \rightarrow (^3F_2, ^3H_6)$ using McCumber theory from the emission spectrum of the $(^3F_2, ^3H_6) \rightarrow ^3H_5$ transition reported in (Shaw et al. 2001) and b) calculated absorption and emission cross-sections for the transition $^3H_5 \rightarrow (^3F_2, ^3H_6)$.

The ground state absorption (GSA) and the ESA absorption of Pr^{3+} doped selenide glass are compared in Fig. 5. GSA absorption was measured for a 500 ppmw Pr^{3+} doped selenide bulk sample (Sakr et al 2014; Sójka et al. 2014;). The estimated contribution of the Se-H impurity band to the GSA was removed using Gaussian fitting (Seddon et al. 2016). The cross section values for

ESA and GSA are very similar. These results are in reasonable agreement with Judd-Ofelt theory which predicts that both transitions have a similar strength. This further confirms the accuracy of the calculation procedure of ESA that was used in this contribution. The spectral distributions of ESA and GSA cross sections have a significant overlap. As a consequence, both transitions can simultaneously absorb the pump energy at wavelengths between approximately 3.7 and 4.3 μm . Thus, the pump energy populates also the level ($^3\text{F}_2, ^3\text{H}_6$) and significantly depletes the upper laser level $^3\text{H}_5$. This behaviour hampers the possibility of establishing population inversion for the $^3\text{H}_5 \rightarrow ^3\text{H}_4$ transition when pumping resonantly between 3.7 and 4.3 μm . Additionally the presence of ESA can result in higher laser thresholds and lower slope efficiencies.

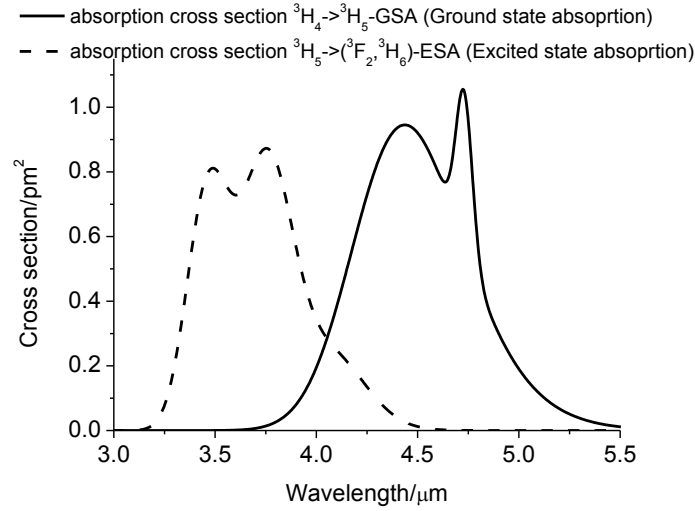


Fig. 5. Absorption cross sections for the $^3\text{H}_5 \rightarrow (^3\text{F}_2, ^3\text{H}_6)$ ESA transition (dashed curve, calculated using McCumber theory) and the $^3\text{H}_4 \rightarrow ^3\text{H}_5$ GSA transition (solid curve, measured but with removal of the contribution of the Se-H impurity band).

4. Results and discussion

In order to study the properties of a resonantly pumped Pr^{3+} doped chalcogenide glass fibre laser, we developed a numerical model. We formulated the rate equations according to the energy-level diagram presented in Fig.1:

$$\frac{dN_3}{dt} = W_{esa}N_2 - (W_{ese} + W_{31} + W_{32})N_3 \quad (3)$$

$$\frac{dN_2}{dt} = (W_{sa} + W_{pa})N_1 - (W_{se} + W_{pe} + W_{21} + W_{esa})N_2 + (W_{ese} + W_{32})N_3 \quad (4)$$

$$N = N_1 + N_2 + N_3 \quad (5)$$

where N_i , $i=1,2,3$ are the ion populations of energy levels and the transition rates W_{xy} are defined in Fig.1.

In the steady state ($\frac{dN_i}{dt} = 0$), the equations (3-5) reduce to three algebraic equations. The power

evolution along the fibre of the pump light P_p and the signal light P_s can be obtained by:

$$\pm \frac{\partial P_p^\pm}{\partial z} = \Gamma_p (\sigma_{pe}N_2 - \sigma_{pa}N_1)P_p^\pm + (\sigma_{ese}N_3 - \sigma_{esa}N_2)P_p^\pm - \alpha_p P_p^\pm \quad (6)$$

$$\frac{dP_s^\pm}{dz} = \pm \Gamma_s (\sigma_{21e}N_2 - \sigma_{21a}N_1)P_s^\pm \mp \alpha_s P_s^\pm \quad (7)$$

where '+' and '-' refer to forward and backward travelling waves, respectively, $P_p^\pm = P_p^+ + P_p^-$;

$$P_s^\pm = P_s^+ + P_s^-$$

and α_p , α_s , represent the background loss coefficient at pump and signal wavelengths, respectively.

In equations (3-5), the stimulated emission or absorption rates are expressed by:

$$W_{xy} = \frac{\Gamma_x \sigma_{xy} \lambda_x P_x}{A h c}$$

(8)

where Γ_x is the confinement factor, which defines the fraction of energy that propagates in the core to the total energy that propagates in the fibre (in the core and the cladding), σ_{xy} is the absorption or emission cross-section for the xy transition, P_x denotes the propagating signal and pump powers, respectively, A is the doping cross section area, h is Planck's constant, λ_x is the wavelength of signal or pump and c is the speed of light in free space. Amplified Spontaneous Emission (ASE) was not included in the laser model. According to Quimby ASE can be neglected in the laser model due to fact that for a laser operation the gain is clamped (Quimby et al. 2008). Further model details can be found elsewhere (Sójka et al. 2012; Sujecki et al. 2015).

Fig. 6 shows the calculated population inversion for the $^3H_5 \rightarrow ^3H_4$ transition (in ions/m³) as a function of the pump intensity for a Pr³⁺ ion density equal to 9.46×10^{24} ions/m³ which corresponds to a 500-ppmw Pr³⁺ doped GeAsGaSe glass. This concentration in a rare earth doped chalcogenide glass does not induce glass crystallisation (Seddon et al. 2010). The pump wavelength is 4.0 μ m, while the laser emission takes place at 4.8 μ m. In order to explore the ESA contribution, the following two cases were considered: (i) including ESA and (ii) with ESA switched off. The results from Fig.6 show that the pump intensity necessary to render the material transparent without including ESA is 34.9 MW/m², while, when the ESA is included, it changes to 57.1 MW/m². We note that the experimentally estimated power damage threshold at 2 μ m for Pr³⁺ doped selenide fibre is in the range of 250 MW/m²; the power damage threshold should increase significantly for longer wavelengths due to better glass transparency (Gattass et al. 2015). Also, it can be seen that the ESA process introduces a large decrease in the value of the population inversion for the $^3H_5 \rightarrow ^3H_4$ transition. For instance, at the pump intensity of 1000 MW/m², the population inversion is approximately halved. These results show clearly that the ESA should be included in the laser model. The main reason for the strong influence of ESA is the long lifetime of the level (3F_2 , 3H_6), thus a large population builds up easily in this level and does not contribute to the amplification process for the $^3H_5 \rightarrow ^3H_4$ transition.

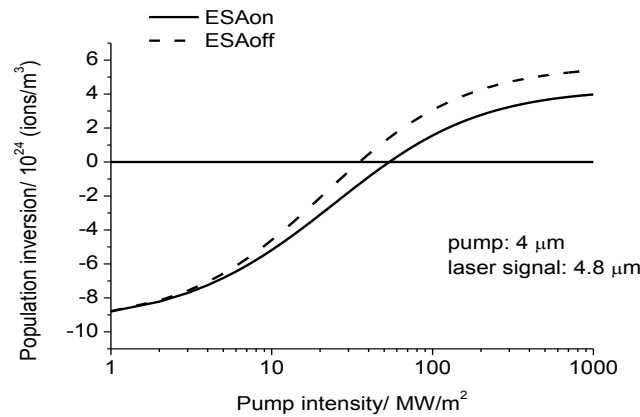


Fig. 6. Calculated population inversion for the $^3H_5 \rightarrow ^3H_4$ transition $\Delta N = N_2 - N_1$ in ions/m³ as a function of the pump intensity for pumping at 4.0 μ m and laser emission at 4.8 μ m. Two cases are considered: (i) without ESA (ESA off) (dashed curve) and (ii) with ESA (ESA on) (continuous curve).

Fig. 7a shows the calculated population inversion (in ions/m³) as a function of the pump intensity for a Pr³⁺ ion density equal to 9.46×10^{24} ions/m³, for different pump wavelengths. The results from Fig. 7a clearly show that detuning the pump wavelength towards longer wavelengths helps reduce the threshold and increase the population inversion for the $^3H_5 \rightarrow ^3H_4$ transition. Additionally, these results show that the maximum population inversion is achieved at a laser pump wavelength of 4.1-4.15 μ m. Therefore the pump wavelength should be selected so that $\sigma_{GSA} > \sigma_{ESA}$

between 3.7-4.2 μm (see Fig. 4). Note that above 4.2 μm there is strong atmospheric absorption band due to CO_2 . Thus, pumping above 4.2 μm is not impossible but impractical. Fig. 7b shows the calculated material gain at 4.8 μm as a function of the pump intensity and wavelength. The results show that the highest gain can be achieved for pumping at 4.1-4.15 μm . Hence the highest values of gain might be obtained by pumping using an appropriate mid-infrared QCL, and this also should help to overcome the experimentally observed loss of chalcogenide glasses in the range of 4.5 μm due to the Se-H impurity absorption band (Tang et al. 2015).

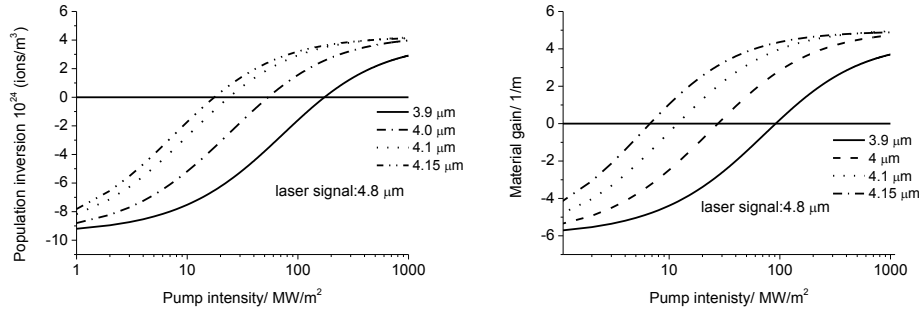


Fig.7. (a) Calculated population inversion $\Delta N = N_2 - N_1$ (in ions/ m^3) for the ${}^3\text{H}_5 \rightarrow {}^3\text{H}_4$ transition and (b) calculated material gain $\Delta N = \sigma_e N_2 - \sigma_a N_1$ both as a function of the pump intensity for different pumping wavelengths and for laser emission at 4.8 μm .

In order to find optimum laser performance, important parameters such as fibre length, output coupling, signal and pumping wavelength were thoroughly investigated. Firstly, the influence of ESA on the laser performance was investigated. The step index fibre (SIF) structure assumed was a single core, with a radius of 15 μm and numerical aperture equal to 0.4. A fibre with a similar a structure has already been reported in the literature (Tang et al. 2015). This fibre structure should enable efficient optical coupling of the QCL pump laser. The fibre modelled (see Table 3) was multi-moded at 5 μm ; in practice a few modes will be guided at 5 μm but through good coupling the number of excited modes can be significantly reduced (Stutzki et al. 2015). The Fundamental Mode (FM) should have the highest confinement factor, *i.e.* the largest optical overlap with the doping region, therefore in the case of lasing this mode should dominate (Stutzki et al. 2015). The fibre laser resonator structure considered uses fibre Bragg gratings (FBGs). The reflectivity of the input FBG for the pump wavelength was assumed to be 0.05 while the reflectivity of this FBG was assumed to be 0.95 for the signal. The output reflectivity is 0.05 for the signal and for the pump it is 0.95. The level of losses assumed for all the wavelengths considered (*i.e.* at the pump and emission wavelengths) is 1 dB/m. The parameters used in the modelling are listed in Table 1, Table 2, Table 3, Fig.4 and Fig.5. These parameters were used in all simulations, unless otherwise stated (Sakr et al. 2014; Sójka et al. 2014; Sujecki et al. 2015).

Table 3. Pr^{3+} doped chalcogenide glass fibre laser modelling parameters.

Quantity	Value	Unit
Ion concentration:	9.46×10^{24}	ions/ m^3
Fibre length:	1	m
Fibre core diameter:	30	μm
Fibre clad diameter:	200	μm
Fibre numerical aperture:	0.4	-
Confinement factor for pump wavelength:	0.9	-

Confinement factor for signal wavelength:	0.9	-
Signal emission cross- section at 4.8 μm :	1.14×10^{-24}	m^2

Fig.8 illustrates the calculated signal output power as a function of fibre length for different pump wavelengths. The pump power was set to 1 W. The laser signal wavelength was set to 4.8 μm . According to numerical simulation this laser emission wavelength (4.8 μm) corresponds to operation at high power. The results presented in Fig.8 are consistent with the results presented in Fig.7. Both results prove that by detuning the pump wavelength from the ESA band the laser output power is increased. It can be observed that when fibre length increases the output power steadily decreases. This phenomenon can be attributed to the signal photon flux reabsorption by $^3\text{H}_4 \rightarrow ^3\text{H}_5$ ground state transition and pump power depletion. Additionally, the laser signal propagating along the fibre is attenuated by the fibre background loss. This causes a reduction in the output power with a further increase in the fibre length. The optical-to-optical efficiencies for 4.8 μm emission with pump wavelengths of 3.9 μm , 4.0 μm , 4.1 μm and 4.15 μm are 22%, 37%, 51% and 55% respectively. Note that the Stokes efficiency limit for a pump wavelength of 4.15 μm is ~86% (Quimby 2006). Moreover, from the results presented in Fig. 8, the optimum fibre length can be estimated. It can be observed that the position of maximum output power shifts to a shorter fibre length for longer pump wavelengths. This difference is due to the larger pump cross section for longer pump wavelengths and the weaker ESA contribution which results in a shorter fibre length and correspondingly smaller attenuation loss. The calculated optical-to-optical efficiencies reported in the literature for chalcogenide fibre lasers doped with Pr^{3+} , Dy^{3+} and Tb^{3+} were below 45% (Quimby et al. 2008; Sójka et al. 2012; Hu et al. 2015; Falconi et al. 2015; Falconi et al. 2016). Therefore resonantly pumping shows a clear advantage in comparison to these previously reported results.

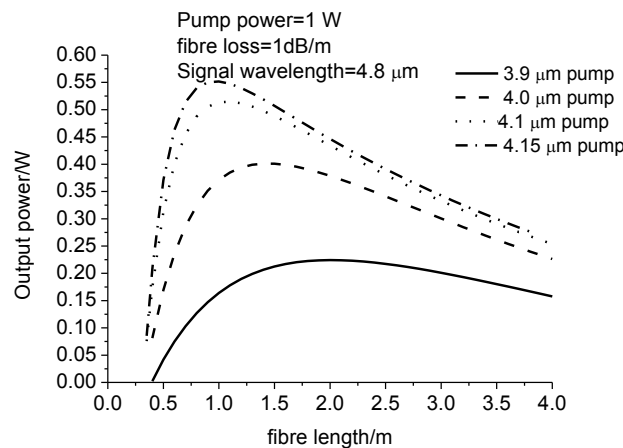


Fig.8. Calculated signal power ($\lambda_s=4.8 \mu\text{m}$) as a function of fibre length with different pump wavelengths. The result were obtained with input pump power $P_p=1 \text{ W}$ and background loss of 1dB/m.

Fig.9 shows the calculated threshold pump power as a function of fibre length for different pump wavelengths. The thresholds for all cases decreases sharply with an increase in the fibre length; they reach the minimum values of 130 mW, 60 mW, 35 mW and 30 mW for pumping at wavelengths of 3.9 μm , 4.0 μm , 4.1 μm and 4.15 μm respectively, and then steadily increase with further increasing fibre length. The high pump power threshold for short fibre length can be attributed to insufficient pump power absorption. For longer fibre lengths the ground state absorption of the $^3\text{H}_4 \rightarrow ^3\text{H}_5$ transition and a background loss in the fibre increases the total cavity loss; thus as a consequence the pump power threshold increases. According to results presented in Fig.8 and Fig.9 it can

concluded that increasing the pump wavelength away from resonance with ESA has a positive effect on the slope efficiency and reduces laser threshold.

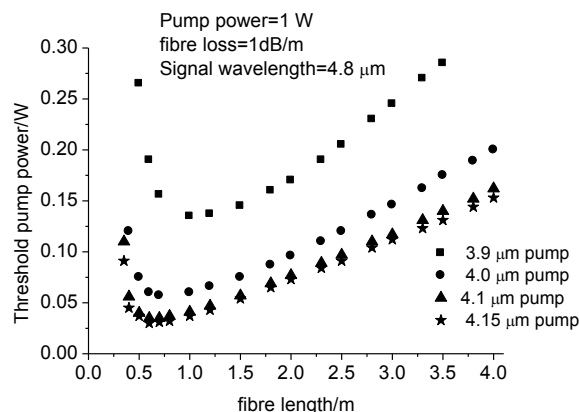


Fig.9. Calculated threshold pump powers as a function of fibre length with different pump wavelengths. The results were obtained with an input pump power $P_p = 1$ W and a background loss of 1dB/m.

In order to estimate the optimum lasing wavelength the output power was calculated as a function of lasing wavelength for various levels of loss (see Fig.10). The input pump power was 1 W at 4.15 μm , and the fibre length was set to 1 metre. It can be observed from Fig. 10 that high output power can be generated by the fibre laser for a spectra region between 4.8-5.2 μm . Therefore a Pr^{3+} doped selenide fibre can be considered as a good candidate for the future construction of a tuneable mid-infrared fibre laser.

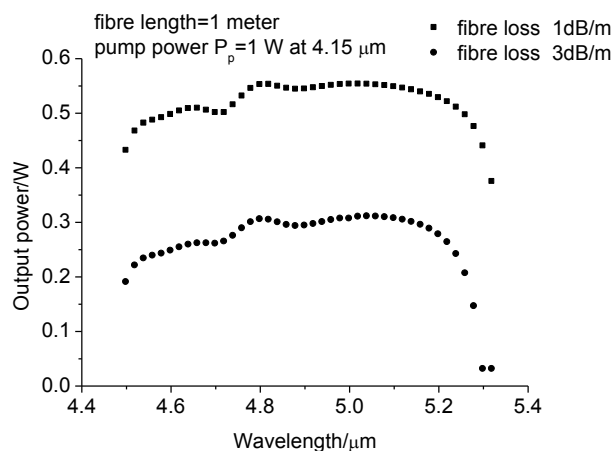


Fig. 10. Calculated output power as a function of lasing wavelength. Results are plotted for a fibre with a background loss of 1dB/m and 3 dB/m, respectively.

In order to illustrate the influence of the output coupling (mirror placed at the opposite end of fibre to the pump launch end) on the laser performance the output power was calculated as a function of output coupler reflectivity. Results are presented in Fig.11. The optimum fibre length of 1 m deduced from the results shown in Fig. 8 and Fig. 9 was used in this simulation, and a 3 dB/m fibre background loss was assumed for all wavelengths. It can be seen that on decreasing the output mirror reflectivity the signal output power increases. The results presented in Fig.11 show that the highest output power can be achieved for an output mirror reflectivity of 0.05 at 4.8 μm . However, a laser cavity based solely on Fresnel reflection at one of the fibre ends (output coupling around ~20%) can ensure a relatively high output power of around 270 mW. Therefore a simple cavity design, that relies on a highly reflective input mirror and the output reflectivity of 20% provided by Fresnel reflection, can also be used in order to achieve efficient laser operation.

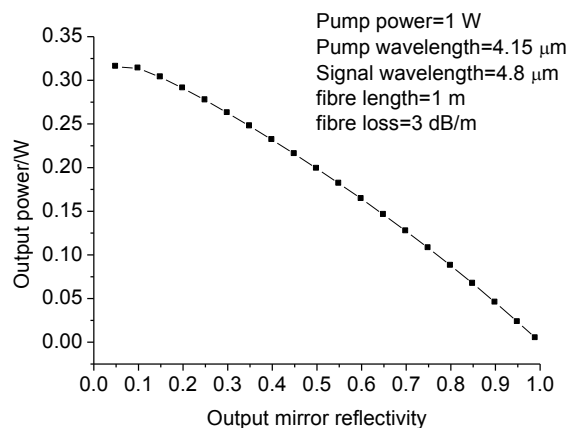


Fig.11. Calculated signal output power as a function of output mirror reflectivity at 4.8 μm .

To make a more comprehensive analysis of the proposed fibre laser, the influence of background loss on laser performance is investigated. The background loss is a limiting factor that hampers the possibility of achieving mid-infrared laser action from selenide doped fibres. Selenide glass possesses high optical absorption loss at wavelengths around 4.5 μm due to Se-H glass impurities. However, recently it has been proven that the loss in this spectral region can be reduced to 1.6 dB/m in the host glass by using sophisticated glass purification techniques (Tang et al. 2015). Calculated output power and threshold pump power as a function of fibre background loss are presented in Fig.12. The fibre length and pump power are set to 1 m and 1 W, respectively. It can be observed that the output power and threshold pump power decrease and increase respectively as the fibre background loss increases. Output power above 100 mW is expected for a fibre loss <5 dB/m. Therefore, in order to obtain efficient laser operation, the fibre loss should be reduced below 5 dB/m.

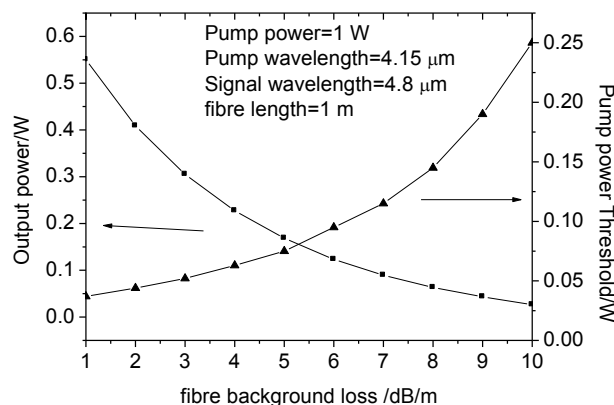


Fig.12. Calculated output power and threshold pump power as a function of fibre background loss; all other parameters (fibre core size *etc.*) are given in Table 3.

5. Conclusions

The performance of resonantly pumped selenide chalcogenide glass fibre lasers doped with Pr^{3+} was comprehensively studied. Particular attention was paid to the role of excited state absorption (ESA), which has not been considered previously in the literature on mid-infrared transitions of Pr^{3+} in selenide chalcogenide glasses. ESA absorption cross section spectra were extracted using McCumber theory. The experimentally extracted parameters formed the basis for the numerical model used in this study. The numerical results showed that ESA had a major influence on the laser performance and that its effect could be reduced by selecting the pump wavelength so that $\sigma_{\text{GSA}} > \sigma_{\text{ESA}}$. It was also shown that a resonant pumping scheme using a high power QCL is a better

solution when compared with the best pumping scheme reported so far. The results obtained showed that resonant pumping allowed for a significant reduction in the laser threshold, and an increase of the laser efficiency. Furthermore, we showed that knowledge of the ESA spectral distribution is indispensable when selecting the optimal wavelength for resonant pumping.

Acknowledgments

This research has been partly supported by the European Commission through the framework Seven (FP7) project MINERVA (317803; www.minerva-project.eu). The authors would like to acknowledge networking support from COST Action: MP1401. LS would like to acknowledge support by the Polish Ministry of Science and Higher Education under the project entitled “Iuventus Plus”, 2016–2018 (project no. IP0441/IP2/2015/73.) Also we acknowledge COST Action MP 1401 supported by the EU Framework Programme Horizon 2020.

References and links

- Caspary R., Applied Rare-Earth Spectroscopy for Fiber Laser Optimization, Shaker, Aachen, 2003, ISBN 3-8322-0315-X
- Chahal, R., Starecki, F., Boussard-Plédel, C., Doualan J-L., Michel, K., Brilland, L., Braud, A., Camy, P., Bureau, B., Nazabal, V., “Fiber evanescent wave spectroscopy based on IR fluorescent chalcogenide fibers”, Sensors and Actuators B: Chemical, Volume 229, 28 June 2016, Pages 209-216
- Falconi, M. C., Scarcia, W., Palma, G., Chahal, R., Starecki, F., Nazabal, V., Troles, J., Adam, J. L., and Prudenzano, F., "Optimization of Mid-IR microstructured fiber laser based on dysprosium doped chalcogenide glass," in *17th International Conference on Transparent Optical Networks (ICTON)*, pp. 1-5(2015)
- Falconi, M. C., Palma, G., Starecki, F., Nazabal, V., Troles, J., Taccheo, S., Ferrari, M., Prudenzano, F., "Design of an Efficient Pumping Scheme for Mid-IR Dy^{3+} :Ga₅Ge₂₀Sb₁₀Sb₆₅ PCF Fiber Laser," Photonics Technology Letters, IEEE, 28, 1984-1987 (2016)
- Ferrier, A., Velázquez, M., Doualan, J.-L. and Moncorgé, R., "Spectroscopic investigation and mid-infrared luminescence properties of the Pr^{3+} -doped low phonon single crystals CsCdBr_3 , KpB_2Cl_5 and Tl_3PbBr_5 ," Journal of Luminescence **129**, 1905-1907 (2009).
- Gattass, R. R., Thapa, R., Kung, F. H., Busse, L. E., Shaw, L. B., and Sanghera, J. S., "Review of infrared fiber-based components," Appl. Opt. **54**, F25-F34 (2015).
- Gomes, L., Librantz, A. F. H. and Jackson, S. D., "Energy level decay and excited state absorption processes in dysprosium-doped fluoride glass," Journal of Applied Physics **107**, 053103 (2010).
- <http://www.pranalytica.com>
- Hu, J., Menyuk, C. R., Wei, C., Shaw, L. B., Sanghera, J. S., and Aggarwal, I. D., "Highly efficient cascaded amplification using Pr^{3+} -doped mid-infrared chalcogenide fiber amplifiers," Opt. Lett. **40**, 3687-3690 (2015).
- Jackson, S. D., "Towards high-power mid-infrared emission from a fibre laser," Nat Photon. **6**, 423-431 (2012).
- Karaksina, E. V., Shiryayev, V.S., Kotereva, T. V., and Churbanov, M. F., "Preparation of high-purity $\text{Pr}^{(3+)}$ doped Ge–Ga–Sb–Se glasses with intensive middle infrared luminescence," Journal of Luminescence **170**, Part 1, 37-41 (2016).
- Karaksina, E. V., Shiryayev, V.S., Kotereva, T. V., Velmuzhov, A. P., Ketkova, L.A., Snopatin, G. E., Preparation of high-purity Pr^{3+} doped Ge–As–Se–In–I glasses for active mid-infrared optics, Journal of Luminescence, Volume 177, September 2016, Pages 275-279, ISSN 0022-2313
- Koepke, C., Wiśniewski, K., Grinberg, M., Russell, D. L., Holliday, K., and G. H. Beall, G. H., "Excited state absorption in Cr^{3+} -doped gahnite glass ceramics," Journal of Luminescence **78**, 135-146 (1998).

- Kozak, M., Goebel, D., Kowalsky, W., and Caspary, R., "Excited state absorption spectroscopy for thulium-doped zirconium fluoride fiber," *Optics Communications* **259**, 154-157 (2006).
- Pollnau, M., and Jackson S., "Advances in Mid-Infrared Fiber Lasers," in *Mid-Infrared Coherent Sources and Applications*, M. Ebrahim-Zadeh, and I. Sorokina, eds. (Springer Netherlands, 2008), pp. 315-346.
- R.S. Quimby, R. S., B.G. Aitken B. G., "Multiphonon energy gap law in rare-earth doped chalcogenide glass", *J. Non-Cryst. Solids*, 320,100 (2003).
- Quimby, R. S, Shaw, L. B., Sanghera, J. S., and Aggarwal, I. D., "Modeling of Cascade Lasing in Dy:Chalcogenide Glass Fiber Laser With Efficient Output at 4.5 μm ," *Photonics Technology Letters, IEEE* **20**, 123-125 (2008).
- Quimby, R. S., and Zheng, B., "New excited-state absorption measurement technique and application to Pr^{3+} doped fluorozirconate glass," *Applied Physics Letters* **60**, 1055-1057 (1992).
- Quimby, R. S, *Photonics and Lasers: an Introduction*, Wiley, (2006).
- Rauter, P., Menzel, S., Goyal, A. K., Wang, C.A., Sanchez, A., Turner, G., and Capasso F., "High-power arrays of quantum cascade laser master-oscillator power-amplifiers," *Opt. Express* **21**, 4518-4530 (2013).
- Sakr, H., Furniss, D., Tang, Z., Sojka, L., Moneim, N.A., Barney, E., Sujecki, S., Benson, T. M., and Seddon, A. B., "Superior photoluminescence (PL) of Pr^{3+} -In, compared to Pr^{3+} -Ga, selenide-chalcogenide bulk glasses and PL of optically-clad fiber," *Opt. Express* **22**, 21236-21252 (2014).
- Seddon, A. B., "A Prospective for new mid-infrared medical endoscopy using chalcogenide glasses," *Int. J. Appl. Glass Sci.* 2(3)177–191 (2011).
- Seddon, A. B., "Mid-infrared (IR) – A hot topic: The potential for using mid-IR light for non-invasive early detection of skin cancer in vivo," *Phys. Status Solidi B* 250(5), 1020–1027 (2013).
- Seddon, A. B., Furniss, D., Tang, Z. Q., Sojka, L., T. M. Benson, T. M., Caspary, R., Sujecki, S., "True mid-infrared Pr^{3+} absorption cross section in a selenide-chalcogenide host-glass" *18th International Conference on Transparent Optical Networks (ICTON)*, (2016)
- Seddon, A., Tang, Z., Furniss, D., Sujecki, S., Benson, T., "Progress in rare-earth-doped mid-infrared fiber lasers," *Opt. Express* 18, 26704-26719 (2010).
- Shaw, L. B, Cole, B., Thielen, P. A., Sanghera, J. S., and Aggarwal, I. D., "Mid-wave IR and long-wave IR laser potential of rare-earth doped chalcogenide glass fiber," *Quantum Electronics, IEEE Journal of* **37**, 1127-1137 (2001).
- Shpotyuk, Y., Boussard-Pledel, C., Nazabal, V., Chahal, R., Ari, J., Pavlyk, B., Cebulski, J., Doualan, J. L, and Bureau, B., "Ga-modified As_2Se_3 -Te glasses for active applications in IR photonics," *Optical Materials* **46**, 228-232 (2015).
- Sójka, L., Tang, Z., Zhu, H., Bereś-Pawlik, E., Furniss, D., Seddon, A. B., T. M. Benson, T. M., and Sujecki, S., "Study of mid-infrared laser action in chalcogenide rare earth doped glass with Dy^{3+} , Pr^{3+} and Tb^{3+} ," *Opt. Mater. Express* **2**, 1632-1640 (2012).
- Sójka, L., Tang, Z., Furniss, D., Sakr, H., Oladeji, A., Bereś-Pawlik, E., Dantanarayana, H., Faber, E., Seddon, A. B., Benson, T. M., and Sujecki, S., "Broadband, mid-infrared emission from Pr^{3+} doped GeAsGaSe chalcogenide fiber, optically clad," *Opt. Mater.* 36(6), 1076–1082 (2014).
- Stutzki, F., Jansen, F., Otto, H.-J., Jauregui, C., Limpert, J., and Tünnermann, A., "Designing advanced very-large-mode-area fibers for power scaling of fiber-laser systems," *Optica* **1**, 233-242 (2014).
- Sujecki, S., Oladeji, A., Phillips, A., Seddon, A. B Benson, T. M., Sakr, H., Tang, Z., Barney, E., Furniss, D., Sójka, L., Bereś-Pawlik, E., Scholle, K., Lamrini, S., and Furberg, P., "Theoretical

study of population inversion in active doped MIR chalcogenide glass fibre lasers (invited)," Opt Quant Electron **47**, 1389-1395 (2015).

Tang, Z., Shiryayev, V. S., Furniss, D., Sojka, L., Sujecki, S., Benson, T. M., Seddon, A. B., and M. F. Churbanov, M. F., "Low loss Ge-As-Se chalcogenide glass fiber, fabricated using extruded preform, for mid-infrared photonics," Opt. Mater. Express **5**, 1722-1737 (2015).

Tang, Z., Furniss, D., Fay, M., Sakr, H., Sójka, L., Neate, N., Weston, N., Sujecki, S., Benson, T. M., and Seddon, A. B., "Mid-infrared photoluminescence in small-core fiber of praseodymium-ion doped selenide-based chalcogenide glass," Opt. Mater. Express **5**, 870-886 (2015).

Tao, G., Ebendorff-Heidepriem, H., Stolyarov, A.M., Danto, S., Badding, J. V., Fink, Y., Ballato, J., and Abouraddy, A. F., "Infrared fibers," Adv. Opt. Photon. **7**, 379-458 (2015).